

NAVAL POSTGRADUATE SCHOOL

Monterey, California



THESIS

HIGH ENERGY LASERS FOR SHIP-DEFENSE AND MARITIME PROPAGATION

by

Vasileios Bouras

December 2002

Thesis Advisor:

William B. Colson

Co-Advisor:

Phillip E. Pace

Approved for public release; distribution is unlimited

THIS PAGE INTENTIONALLY LEFT BLANK

REPORT DOCUMENTATION PAGE			Form Approved OMB No. 0704-0188	
Public reporting burden for this collection of information is estimated to average 1 hour per response, including the time for reviewing instruction, searching existing data sources, gathering and maintaining the data needed, and completing and reviewing the collection of information. Send comments regarding this burden estimate or any other aspect of this collection of information, including suggestions for reducing this burden, to Washington headquarters Services, Directorate for Information Operations and Reports, 1215 Jefferson Davis Highway, Suite 1204, Arlington, VA 22202-4302, and to the Office of Management and Budget, Paperwork Reduction Project (0704-0188) Washington DC 20503.				
1. AGENCY USE ONLY (Leave blank)		2. REPORT DATE December 2002	3. REPORT TYPE AND DATES COVERED Master's Thesis	
4. TITLE AND SUBTITLE: High Energy Lasers for Ship-Defense and Maritime Propagation			5. FUNDING NUMBERS	
6. AUTHOR(S) Bouras Vasileios				
7. PERFORMING ORGANIZATION NAME(S) AND ADDRESS(ES) Naval Postgraduate School Monterey, CA 93943-5000			8. PERFORMING ORGANIZATION REPORT NUMBER	
9. SPONSORING /MONITORING AGENCY NAME(S) AND ADDRESS(ES) N/A			10. SPONSORING/MONITORING AGENCY REPORT NUMBER	
11. SUPPLEMENTARY NOTES The views expressed in this thesis are those of the author and do not reflect the official policy or position of the Department of Defense or the U.S. Government.				
12a. DISTRIBUTION / AVAILABILITY STATEMENT Approved for public release; distribution is unlimited			12b. DISTRIBUTION CODE	
13. ABSTRACT (maximum 200 words) <p>High Energy Lasers (HELs) are a new class of weapons that may be of great value to the Navy in the near future. A high-power Free Electron Laser (FEL) is being designed using short Rayleigh-length resonators to increase the spot size at the mirrors and hence avoid mirror damage. Three-dimensional simulations are used to study the effects of an electron beam misalignment (electron beam tilt). This thesis shows that the proposed design is tolerant of typical electron beam misalignments. The performance of a step-tapered undulator is also studied for the 100 kW proposed upgrade of the Jefferson Laboratory FEL. The results of this research show that the gain is above the required threshold for the 100 kW design while the energy spread does not change significantly over any undulator design. The spectrum of the proposed FEL shows that most of the power is concentrated around the fundamental frequency. It is shown in this thesis that smooth FEL pulses can significantly reduce the negative effects of absorption and scattering. Recent HEL science and technology developments are discussed for both Free Electron and Solid-State Lasers.</p>				
14. SUBJECT TERMS Free Electron Laser, Solid-State Lasers, High Energy Lasers, Short Rayleigh Length, Step-Taper Undulator, SSHCL, Laser Propagation			15. NUMBER OF PAGES 110	
			16. PRICE CODE	
17. SECURITY CLASSIFICATION OF REPORT Unclassified	18. SECURITY CLASSIFICATION OF THIS PAGE Unclassified	19. SECURITY CLASSIFICATION OF ABSTRACT Unclassified	20. LIMITATION OF ABSTRACT UL	

THIS PAGE INTENTIONALLY LEFT BLANK

Approved for public release; distribution is unlimited

**HIGH ENERGY LASERS FOR SHIP-DEFENSE AND MARITIME
PROPAGATION**

Vasileios Bouras
Lieutenant, Hellenic Navy
B.S., Hellenic Naval Academy, 1993

Submitted in partial fulfillment of the
requirements for the degree of

**MASTER OF SCIENCE IN APPLIED PHYSICS
MASTER OF SCIENCE IN ELECTRICAL ENGINEERING**

from the

**NAVAL POSTGRADUATE SCHOOL
December 2002**

Author: Vasileios Bouras

Approved by: William B. Colson
Thesis Advisor, Department of Physics

Phillip E. Pace
Co-Advisor, Department of Electrical and Computer Engineering

Joseph Blau
Second Reader, Department of Physics

William B. Maier II
Chairman Department of Physics

John P. Powers
Chairman, Department of Electrical and Computer Engineering

THIS PAGE INTENTIONALLY LEFT BLANK

ABSTRACT

High Energy Lasers (HELs) are a new class of weapons that may be of great value to the Navy in the near future. A high-power Free Electron Laser (FEL) is being designed using short Rayleigh-length resonators to increase the spot size at the mirrors and hence avoid mirror damage. Three-dimensional simulations are used to study the effects of an electron beam misalignment (electron beam tilt). This thesis shows that the proposed design is tolerant of typical electron beam misalignments. The performance of a step-tapered undulator is also studied for the 100 kW proposed upgrade of the Jefferson Laboratory FEL. The results of this research show that the gain is above the required threshold for the 100 kW design while the energy spread does not change significantly over any undulator design. The spectrum of the proposed FEL shows that most of the power is concentrated around the fundamental frequency. It is shown in this thesis that smooth FEL pulses can significantly reduce the negative effects of absorption and scattering. Recent HEL science and technology developments are discussed for both Free Electron and Solid State Lasers.

THIS PAGE INTENTIONALLY LEFT BLANK

TABLE OF CONTENTS

I.	INTRODUCTION	1
II.	HEL WEAPON TECHNOLOGY.....	7
A.	FEL DESIGN	7
B.	FEL CRITICAL COMPONENTS	8
1.	Injector.....	8
2.	Accelerator	10
3.	Wiggler.....	11
4.	Resonator	13
C.	MW-CLASS FEL PROPOSED DESIGN	13
D.	SSL DESIGN	14
E.	CHALLENGES FOR MW-CLASS SSL.....	15
1.	Laser Diodes.....	15
2.	Phasing of Laser Modules (Fiber Lasers).....	16
3.	Thermal Control of Laser Media	17
F.	HEAT CAPACITY LASER.....	19
G.	CONCLUSIONS	22
III.	PHYSICS OF SOLID-STATE AND FREE ELECTRON LASER	23
A.	PHYSICS BEHIND SOLID STATE LASERS	23
1.	Einstein A and B Coefficients	23
a.	<i>Absorption</i>	23
b.	<i>Spontaneous Emission</i>	24
c.	<i>Stimulated Emission</i>	24
2.	Atomic Lineshapes.....	25
a.	<i>The Homogeneous Broadened Line</i>	26
b.	<i>The Inhomogeneous Broadened Line</i>	26
3.	Amplification in a Laser.....	26
4.	Population Inversion	28
a.	<i>The Three-Level System</i>	29
b.	<i>The Four-Level System</i>	29
5.	Solid-State Laser Materials	30
a.	<i>Host Materials</i>	30
b.	<i>Active Ions</i>	31
B.	PHYSICS BEHIND FREE ELECTRON LASERS.....	31
1.	Electron Motion	32
2.	Energy Exchange	33
3.	Resonance Condition	33
4.	FEL Pendulum Equation.....	35
5.	Phase Space Analysis	36
6.	FEL Wave Equation	38
7.	Optical Gain	40
8.	Efficiency	41

IV.	SIMULATIONS OF HIGH-POWER FREE ELECTRON LASERS	43
A.	INTRODUCTION	43
1.	Optical Cavities.....	43
2.	Gaussian Modes	44
3.	Resonator Optics with a Short Rayleigh Length.....	44
B.	HIGH-POWER FEL DESIGN PARAMETERS.....	45
C.	BETATRON MOTION (LINEAR UNDULATOR).....	47
D.	SIMULATION METHODS.....	48
E.	SIMULATION RESULTS	51
1.	Tilting about the Center of the Undulator ($t_\beta = 0.5$)	51
2.	Tilting at the Beginning of Undulator ($t_\beta = 0$)	54
F.	CONCLUSIONS	57
V.	SIMULATIONS OF 100 KW FEL USING A STEP-TAPERED UNDULATOR.....	59
A.	INTRODUCTION	59
1.	Short Pulses.....	59
2.	Tapered Undulator	60
B.	100 KW FEL DESIGN	61
C.	WEAK FIELD GAIN	61
D.	ENERGY SPREAD	62
E.	CONCLUSIONS	63
VI.	POWER SPECTRUM OF THE FEL	65
A.	FOURIER TRANSFORM OF A LASER PULSE TRAIN.....	65
B.	POWER DISTRIBUTION	68
1.	Microwave Regime	69
2.	Visible Spectrum	70
C.	ATMOSPHERIC EFFECTS	72
1.	Power Removal (Pulse Distortion)	73
2.	Thermal Blooming	75
D.	GAUSSIAN SHAPE PULSES	75
E.	CONCLUSIONS	77
VII.	CONCLUSIONS	79
	LIST OF REFERENCES	81
	INITIAL DISTRIBUTION LIST.....	85

LIST OF FIGURES

Figure 1.1.	SS-NX-27 Novator Alfa. (From [Ref. 1])	1
Figure 1.2.	Naval Threat Suite.	2
Figure 1.3.	Thermal Blooming (Due to Atmospheric Absorption) and Scattering Effects. (From [Ref. 1])	4
Figure 2.1.	Typical Elements of an FEL (Regenerative Amplifier). (From [Ref. 6]).....	8
Figure 2.2.	FEL Critical Components. (From [Ref. 1])	12
Figure 2.3.	Schematic Diagram of a MW Level FEL Weapon System. (From [Ref. 12]).....	14
Figure 2.4.	Elements of a Typical Solid State Laser.	15
Figure 2.5.	Schematic of a zig-zag slab Laser. (a) Slab geometry, (b) End view, (c) Optical path in y-z plane. (After [Ref. 14])	18
Figure 2.6.	Heat Capacity Laser Concept. (From [Ref. 6]).....	20
Figure 2.7.	LLNL 100 kW SSHCL Design. (From [Ref. 1])	21
Figure 2.8.	SSHCL 100 kW Demonstration Concept for the Army. (From [Ref. 3])	22
Figure 3.1.	Simplified Energy Diagram of a Three-Level Laser. (From [Ref. 14])	28
Figure 3.2.	Simplified Energy Diagram of a Four-Level Laser. (From [Ref. 14])	28
Figure 3.3.	Resonance Condition. One Wavelength of Light (Traveling at Speed c), Passes over an Electron (Traveling at Speed $\mathbf{b}_z c$), as the Electron Travels Through One Undulator Wavelength.	34
Figure 3.4.	Electron Evolution in Phase Space, Optical Field Gain $G(\mathbf{t})$ and Phase $\mathbf{j}(\mathbf{t})$ for a Single Pass through the Undulator with Electrons Injected at Resonance ($\mathbf{n}_o = 0$)	37
Figure 3.5.	Electron Evolution in Phase Space, Optical Field Gain $G(\mathbf{t})$ and Phase $\mathbf{j}(\mathbf{t})$ for a Single Pass through the Undulator with Electrons Injected Slightly Off Resonance $\mathbf{n}_o = 2.6$	38
Figure 4.1.	Geometry of Spherical Mirror Resonator. R_1 , R_2 are the Radiuses of Curvature of the Two Mirrors.....	43
Figure 4.2.	Expansion of a Gaussian Beam.	44
Figure 4.3.	Concentric Cavity, $R_1 = R_2 = S/2$	45
Figure 4.4.	MW Level FEL Design.	46
Figure 4.5.	Three-Dimensional Simulation Results for the Proposed MW FEL with a Short Rayleigh Length and a Narrow Electron Beam Injected without an Offset in Position or Angle ($y_o = 0, \mathbf{q}_{yo} = 0$). At Saturation, the Efficiency Reaches $\mathbf{h} = 2.5\%$	50
Figure 4.6.	Electron Beam Tilt ($\mathbf{t}_b = 0.5$)	51
Figure 4.7.	Single-Pass Extraction Efficiency, \mathbf{h} vs Initial Phase Velocity v_o for Different Values of \mathbf{q}_{yo} through the Undulator Center ($\mathbf{t}_b = 0.5$).	52

Figure 4.8.	Peak Single-Pass Extraction Efficiency, \hat{h} vs. Normalized Electron Beam Tilt q_{yo} through the Center of Undulator ($t_b = 0.5$). The Required Efficiency for 1 MW Goal (0.7%) is Achieved for Tilt Angles Less than 6mrad.	53
Figure 4.9.	Three-Dimensional Simulation Results for an Injected Electron Beam with an Initial Tilt $q_{yo} = 4$ ($t_b = 0.5$). Efficiency Decreases to $h = 2.1\%$	54
Figure 4.10.	Electron Beam Tilt ($t_b = 0$).....	54
Figure 4.11.	Single-Pass Extraction Efficiency, h vs Initial Phase Velocity v_o for Three Different Values of q_{yo} Occurred at the Beginning of the Undulator ($t_b = 0$).	55
Figure 4.12.	Peak Single-Pass Extraction Efficiency, \hat{h} vs. Normalized Electron Beam Tilt q_{yo} at the Undulator Entrance ($t_b = 0$). The Efficiency for 1 MW Goal (0.7%) is Achieved for Tilt Angles Less than 1mrad.	56
Figure 4.13.	Three-Dimensional Simulation Results for an Injected Electron Beam with an Initial Tilt $q_{yo} = 1$ ($t_b = 0$). Efficiency Oscillates between 1% and 2%.	57
Figure 5.1.	Schematic for a Step-Taper Undulator	60
Figure 5.2.	Weak Field Gain G Versus Desynchronism for Step Taper with $Q_n = 4.2$. Gain Above Threshold for All Cases, Optimum Gain with No Taper ($\Delta = 0$).	62
Figure 5.3.	Energy Spread $\Delta g/g$ Versus Desynchronism For Step Taper with $Q_n = 4.2$. Induced Energy Spread does not Change Much with any Undulator Design.	63
Figure 6.1.	FEL Output Pulse Train.	65
Figure 6.2.	Power Spectrum around 1 μm (a), Main Lobe (b).	68
Figure 6.3.	Normalized Power Spectral Density of the FEL Beam.	69
Figure 6.4.	Power Spectra in Microwave Regime.	70
Figure 6.5.	Power Spectral Density in the Visible Region.	70
Figure 6.6.	Scattered Power in the Visible Spectra.	71
Figure 6.7.	Aerosol Scattering. (From [Ref. 1]).....	72
Figure 6.8.	Maritime Aerosol Model (23 km Visibility). (After [Ref. 24])	73
Figure 6.9.	Power Removal.....	74
Figure 6.10.	A CW Pulse with (a) Rectangular Envelope (in Blue), (b) Using a Hanning Pulse (in Red).....	76
Figure 6.11.	Normalized Power Spectra Density of a micropulse (a) Rectangular Envelope (in Blue), (b) Hanning Pulse (in Red).....	77

LIST OF TABLES

Table 4.1.	High-Power FEL Parameters.....	46
Table 5.1.	100 kW FEL Parameters.....	61

THIS PAGE INTENTIONALLY LEFT BLANK

LIST OF SYMBOLS

\vec{A}	Magnetic vector potential
A	Fourier Transform of signal \tilde{a}
A_{21}	Einstein coefficient for spontaneous emission
a	Dimensionless optical field
a_o	Initial dimensionless optical field
\mathbf{a}_k	Fourier series coefficients
\hat{a}	Peak amplitude of optical field signal
a_e	Extinction coefficient
a_{sc}	Scattering coefficient
\vec{B}_u	Undulator magnetic field
\vec{B}_s	Optical magnetic field
\vec{B}_L	Linear undulator magnetic field
B	RMS magnetic field
B_{12}	Einstein coefficient for absorption
B_{21}	Einstein coefficient for stimulated emission
\vec{b}	Dimensionless relativistic electron velocity
\vec{b}_\perp	Dimensionless relativistic electron velocity in the transverse direction
b_z	Dimensionless relativistic electron axial velocity
c	Speed of light in vacuum

c_s	Speed of light in solids
\boldsymbol{g}	Lorentz factor
\boldsymbol{g}_o	Gain coefficient (solid-state lasers)
d	Dimensionless value of desynchronism
dV	Differential volume
df	Signal bandwidth
Δ	Step taper rate
$\Delta \boldsymbol{g} / \boldsymbol{g}$	Energy spread
$\Delta K / K$	Step change in undulator parameter
ΔE_e	Change in energy of a single electron
Δf	Transition linewidth (solid-state lasers)
$\Delta \boldsymbol{n}$	Change in phase velocity of an electron
\vec{E}_s	Optical electric field
E	Electric field amplitude
E_i	i_{th} energy level
E_a	Energy contained in signal \tilde{a}
e	Electron charge
\boldsymbol{e}_n	Electron beam emittance
F	Filling factor
f	Frequency
f_o	Fundamental frequency
\boldsymbol{f}	Initial phase of optical wave

G	Optical field single-pass gain
$g_{1,2}$	Degeneracy parameters
g	Lineshape function (solid-state lasers)
h	Planck's constant
\mathbf{h}	Single-pass extraction efficiency
$\hat{\mathbf{h}}$	Peak single-pass extraction efficiency
I_{peak}	Peak current
I_{avg}	Average current
I_f	Optical intensity at frequency f (solid-state lasers)
\vec{J}_{\perp}	Transverse electron beam current
j	Dimensionless current density
k	Optical wavenumber
k_o	Undulator wavenumber
K	Undulator parameter
KE	Kinetic energy of the electron beam
l_e	Electron pulse length
L	Undulator length
λ	Optical wavelength
λ_o	Undulator wavelength
m	Electron mass
N	Number of undulator periods
N_i	Population density of the i th state

n	Index of refraction
v	Dimensionless electron phase velocity
v_o	Dimensionless initial electron phase velocity
P	Power
Π	Rectangular pulse shape function
Q_n	Resonator quality factor
q	Electron bunch charge
R_i	Curvature of i_{th} mirror
r_e	Electron beam radius
\mathbf{r}	Current density
\mathbf{r}_s	Radiation density (solid-state lasers)
S	Resonator cavity length
\mathbf{s}_x	Dimensionless electron beam radius
\mathbf{s}_z	Dimensionless electron pulse length
\mathbf{s}	Stimulated emission cross-section area (solid-state lasers)
t	Time
T	Optical pulse period
T_o	Pulse width
t	Dimensionless time
t_w	Dimensionless position of optical waist
t_b	Dimensionless position of electron beam tilting
t_{ij}	Photon lifetime – Relaxation time

\mathbf{u}	Electron velocity
w	Normalized beam width
w_o	Dimensionless optical waist radius
W_o	Characteristic optical mode radius
W_{ij}	Pumping rate between i_{th} and j_{th} level (solid-state lasers)
\mathbf{w}	Angular frequency
w_o	Fundamental angular frequency
w_b	Dimensionless betatron frequency
W	Pulse repetition rate
\mathbf{q}	Electron beam tilt
\mathbf{q}_{yo}	Initial beam tilt in y-direction
Θ	Step function
y_o	Electron beam offset
\mathbf{y}	Phase of the optical wave
z_o	Dimensionless Rayleigh length
Z_o	Rayleigh length
\mathbf{z}	Dimensionless electron phase

THIS PAGE INTENTIONALLY LEFT BLANK

ACKNOWLEDGMENTS

I would first like to thank my parents, George and Panagiota Boura, for instilling in me the desire to always strive to learn and to do my best. I would like to thank my Professor Bill Colson, an outstanding teacher and humanitarian. I also want to thank Prof. Joe Blau and Prof. Peter Crooker for always assisting me without hesitation throughout this study. Finally I want to thank my lovely wife Marina without whose love, support and constant encouragement, I could never have completed this program.

THIS PAGE INTENTIONALLY LEFT BLANK

EXECUTIVE SUMMARY

High Energy Lasers (HELs) have two characteristics that make them particularly valuable for ship self-defense: they are extremely fast and extremely precise. In addition to the potential of using high-energy lasers against moderately hard targets, laser systems could have the potential for lethal precision engagement against classes of soft targets, including personnel and light vehicles. The high power Free-Electron Lasers (FELs) and Solid-State Lasers (SSLs) are the most likely candidates for developing a Navy high-energy weapon system.

SSL technology, including fiber-laser technology, is often presented as the enabling technology for new HEL tactical missions. However, thermal control is the bane of all SSL systems, since the increase in temperature distorts the lasing medium. Thus, efficient thermal control of laser media needs to be pursued. Of all the solid-state laser concepts, probably the closest to achieving 100 kW level output power is the heat capacity laser (SSHCL), where lasing and cooling occur separately to avoid the growth of temperature gradients across the active area preserving beam quality.

FELs can produce powerful, highly coherent, optical beams but also place extreme demands on the resonator mirrors. A critical challenge for FELs is to maintain or even improve electron beam brightness as the beam current is increased. Another concern for FELs is making them compact and rugged enough to meet shipboard packaging requirements.

A high power free electron laser for ship defense is being designed at the Naval Postgraduate School in collaboration with Jefferson Laboratory. A short Rayleigh length resonator has been proposed to increase the spot size at the mirrors, and hence reduce mirror damage while meeting shipboard packaging requirements. This implies a nearly concentric cavity with a very small optical mode waist. A slight misalignment of the electron beam, either an offset or a tilt, could conceivably reduce the overlap between the electrons and the optical mode in the center of the undulator, resulting in less gain and efficiency. Three-dimensional simulations showed that the proposed design is tolerant of

typical electron beam misalignments (either an electron beam tilt or an offset), providing enough efficiency for the MW level weapon system requirements.

One transitional step toward the 1 MW output power required for a laser weapon is the proposed 100 kW upgrade of the Jefferson Laboratory FEL. Additional simulations were conducted to explore the use of a step-tapered undulator, which alters the resonance condition halfway through the undulator, in order to improve the FEL performance. The results of this research showed that step-taper is not always so effective; however, in all cases explored, the weak field gain was found to be above the required threshold of 21% for the 100 kW design. The induced energy spread at saturation in strong fields did not change significantly over any undulator design.

The spectrum and the power distribution of the proposed FEL output were also studied. Approximately 90% of the total power of the laser beam is concentrated in the main lobe (around 1 μm wavelength), while significant amount of power is contained to higher and lower harmonics due to short pulses. Atmospheric absorption and scattering were also studied for a specific maritime aerosol model showing the amount of power that is delivered through the atmosphere over a distance of 5 km.

I. INTRODUCTION

The primary Navy mission for a modern weapon system is cruise missile self defense. Cruise missiles have increasingly sophisticated capabilities and represent a very significant threat to present and future Naval operations. The supersonic cruise missile threat to Naval vessels, such as the SS-NX-27 Novator Alfa is well known and shown in Figure 1.1. The potential engagement time is limited given the distance to the horizon and speeds greatly exceeding Mach 1.

This threat is compounded by the post-Cold War mission shift of Naval operations from predominantly “blue water” activities to now include littoral environments. The greatest evidence of this shift is the “Littoral Combat Ship” (LCS) concept, which has been adopted and is under development by the U.S. Navy. This project involves the building of a new type of ship with warfighting capabilities optimized for versatility in the littorals. It must have self-defense systems enabling it to survive threats such as small boats, patrol craft, low-slow flyers and shore artillery. The priority of this mission is enhanced by recent terrorist actions, such as the USS COLE incident, and ongoing terrorist threats. A high-energy laser (HEL) weapon system is an excellent candidate to fulfill this diverse role.

(UNCLASSIFIED)



Length x Diameter x Wingspan	8.22 m x 0.533 m x 3.1 m
Range	220 km
Speed	Mach 0.6 to 0.8 subsonic Mach 2.9 supersonic
Payload	200 kg
Guidance	GPS, Inertial and active radar homing

Figure 1.1. SS-NX-27 Novator Alfa. (From [Ref. 1])

Two characteristics of the HELs make them particularly valuable for ship self-defense: they are extremely fast and extremely precise. The laser begins its attack within seconds of detecting its target and completes its destruction a few seconds later. In addition to using high-energy lasers against moderately hard targets, laser systems could

have the potential for lethal precision engagement against soft targets, such as personnel, light vehicles, communications, etc. Overall, HELs have the potential to change future military operations in dramatic ways and add a new dimension to a wide range of missions. See Figure 1.2.

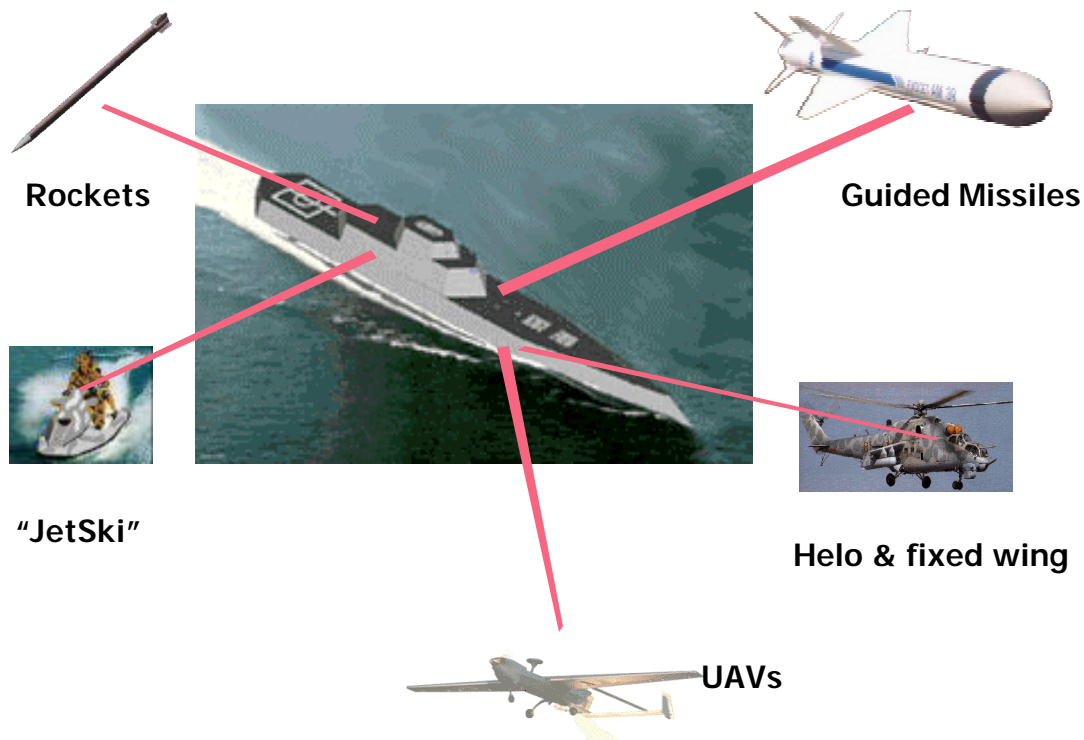


Figure 1.2. Naval Threat Suite.

Greece, the only state in the Balkans and the Eastern Mediterranean that is a participant in both NATO and the European Union, is situated in a very difficult geographic position and is surrounded by sources of tension and engagement. The Hellenic warships must be capable of operating under any possible environmental scenario as part of NATO forces, including open seas and coastal environments.

Moreover, the peculiar geographical structure of Greece, composed of extensive coasts with numerous natural ports and bays as well as a great number of islands and islets, makes the coastal Naval operations absolutely essential to national security. Therefore, all of the previously mentioned threats are relevant to Greece. Thus, the idea

of using Directed Energy Weapons (DEW) appears very appealing to Greece and the Hellenic navy.

At this point, some critical factors must be taken into consideration. The prime power requirement for such a weapon is estimated to be of the order of 10 MW, which is far beyond the power available from the Hellenic warships (3 MW). Also, the possible cost is expected to exceed \$50 million [Ref. 2]. Especially at the beginning of production, this cost is much greater than conventional weapons.

However, even though this may presently be unfeasible, the DEW concept may be a relevant and serious challenge for Greece and other countries during the next few decades.

The high power Free-Electron Lasers (FELs) and Solid-State Lasers (SSLs) are the likely candidates for developing a Navy high-energy weapon system. The U.S. Navy is closely watching the continued efforts of the Army and the Air Force in chemical-laser source development, but intends to focus its source-development efforts on electric-powered laser devices, such as solid-state and free-electron lasers for the following three reasons [Ref. 3]:

- the inherent dangers associated with the storage of chemicals on board ship
- the need to develop a source at the appropriate wavelength for maritime propagation
- the Navy's recent decision, early in 2000, to adopt an electric drive propulsion system for DD-21 and follow-on ships

Though both offer the benefits of using electrical pumping mechanisms, they each have challenges unique to their design. The solid-state lasers will need to overcome the thermal loading that a multi-megawatt system will place in the laser medium. The free-electron laser source will require high average current injector work, as well as work on high-power optical resonator mirrors and an electron beam transport system.

There are also several challenges related to atmospheric effects and propagation in developing a high-energy laser weapon system that will operate in a maritime environment. The atmosphere just above the ocean is very different from the atmosphere

over land, and will require the selection of the appropriate wavelength, power level and pulse format in order to deliver a lethal amount of energy to the target.

Absorption scattering and thermal blooming effects are the primary causes for loss of energy in this environment. See Figure 1.3. In reality, maritime conditions at a particular geographic location and at a particular time may favor different wavelengths on different days. This variable nature of maritime conditions provides a significant advantage to the free-electron laser. The ability of a free electron laser to select different wavelengths is an important capability for a maritime laser.

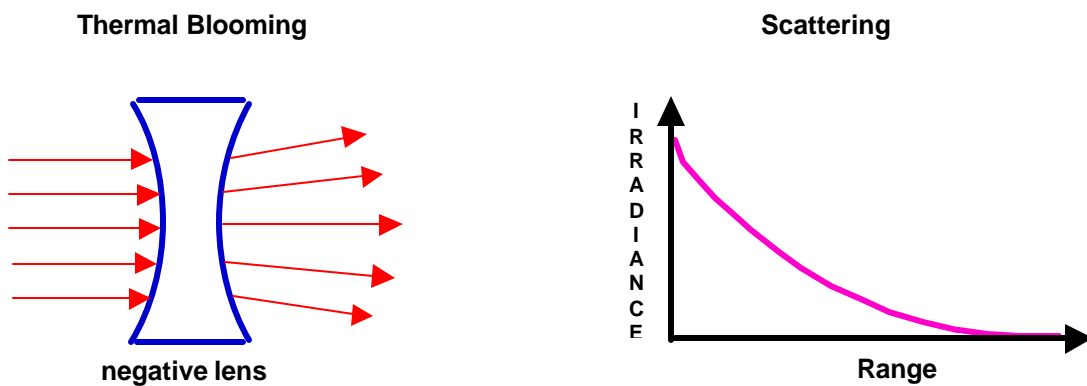


Figure 1.3. Thermal Blooming (Due to Atmospheric Absorption) and Scattering Effects. (From [Ref. 1])

Chapter II of this thesis describes the current initiatives as well as science and technology needs to achieve weapon-class high-energy lasers and presents an overall comparison between the two technologies.

Chapter III of the thesis gives an overview of the theoretical background and discusses the physics behind the Solid-State-Laser and the Free-Electron-Laser.

Chapter IV describes the results of simulations for the 1 MW FEL. This work was presented at the 24th International FEL Conference in Chicago (9/2002) [Ref. 4].

Chapter V describes the results of simulations for the 100 kW upgrade Jefferson Laboratory FEL as a transitional step for the development of a 1 MW which were presented at the 23rd International FEL Conference in Darmstadt Germany (8/2001) [Ref. 5].

Chapter VI presents the power distribution of a short pulse FEL beam over the frequency spectrum and studies the effects of atmospheric absorption and scattering in the performance of FEL as a weapon system.

Chapter VII summarizes the conclusions of this thesis.

THIS PAGE INTENTIONALLY LEFT BLANK

II. HEL WEAPON TECHNOLOGY

Solid-state-laser technology, including fiber-laser technology, is often presented as the enabling technology for new HEL missions, and in particular, tactical missions. However, thermal control is the bane of all SSL systems since the increase in temperature distorts the lasing medium. Thus, efficient thermal control of laser media needs to be pursued. Other technology efforts for high energy include the design and manufacturing of reliable diode pump lasers, and the phasing of laser modules.

The Free-Electron-Laser (FEL) is an all-electric laser that is a competitor to the solid-state laser. A recent demonstration of its 2.1 kW average power [Ref. 1] has put the FEL in the same category as the state-of-the-art solid-state lasers. To obtain more power from an FEL, the energy in the electron beam only needs to be increased by increasing the average current.

Theoretical calculations have shown that FELs have the potential to scale to multi-megawatts. There are, however, many technical challenges to developing a high power FEL. A critical challenge is maintaining, or even, improving electron beam brightness as current in the beam is increased. Another concern for FELs is making them compact and rugged enough to meet shipboard packaging requirements.

A. FEL DESIGN

A Free Electron Laser (FEL) is a device that extracts kinetic energy from a relativistic electron beam and converts it into electromagnetic radiation. This is accomplished by sending relativistic free electrons (not bound to atoms) through a periodic magnetic field produced by a device called an “undulator” or “wiggler”. The spatially periodic magnetic field induces transverse forces on the electrons and causes them to produce electromagnetic radiation in the forward direction of the electron beam. Free Electron Laser (FEL) oscillators couple out a small portion of the radiation with low gain per pass and store the rest. FEL amplifiers couple out most of the radiation with gain per pass. FELs have been demonstrated to provide an electrically driven, powerful source of wavelength selectable, coherent electromagnetic radiation.

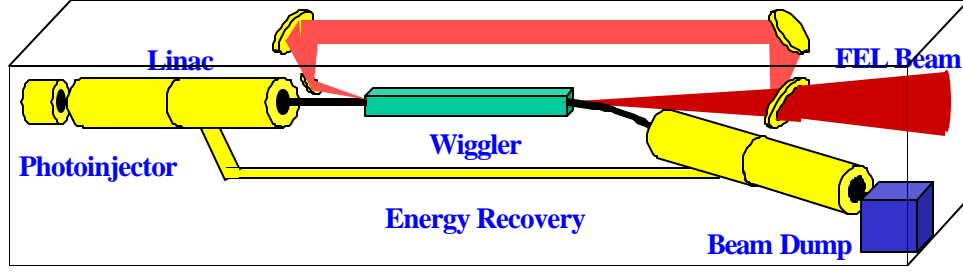


Figure 2.1. Typical Elements of an FEL (Regenerative Amplifier). (From [Ref. 6])

The basic building blocks of a typical FEL as illustrated in Figure 2.1 are

- A source of free electrons (Photoinjector)
- An RF accelerator (Linac), which accelerates the electrons to nearly the speed of light
- A wiggler, using a periodic magnetic field so the electrons emit pulses of electromagnetic radiation
- An optical resonator which outcouples a small portion of the radiation and recirculates the electron beam
- An electron beam decelerator or dump, which safely captures the remaining energy from the electron beam

Very significant progress in FEL technology has been achieved over the past five years and a credible path to a MW-class weapon system demonstration is being defined. The critical component issues for the FEL development are high-average-power injectors, high-current electron beam transport, high-power oscillator and amplifier designs, and high-peak-power density in the optical resonators.

B. FEL CRITICAL COMPONENTS

1. Injector

The purpose of the injector is to produce short, periodic bursts (pulses) of electrons and feed them into the accelerator. During the pulses, typical peak injector currents are in the 1 to > 100 amp range with pulse widths ranging from 1 – 50 ps [Ref. 7]. The average power of the electron beam is increased by increasing the charge in a pulse, the repetition rate of these pulses, or the energy of the electrons. The average current is given by

$$I_{avg} = I_{peak} \frac{T_o}{T} = \frac{q}{T_o} \frac{T_o}{T} = qW, \quad (2.1)$$

where q is the charge per pulse, T_o the pulse duration, T is the pulse period and $W = 1/T$ the repetition rate. To achieve megawatt level average power from an FEL, the injector current (charge per bunch x repetition rate) must be in the range of a half amp to a few amps. Thus, the development of high power injectors seems to be a key issue for a high power FEL.

The injector energy is not recoverable in the accelerator. From this point of view, low-energy injectors are preferred. To date, most have been thinking in terms of a 10-MeV injector [Ref. 8]. Given an average current of 0.375 A, the required RF power is correspondingly 3.75 MW, which is a large amount of un-recoverable energy for 10% wall plug efficiency (~10 MW) in an FEL design. There is a payoff in principle by going down to, say, 5 MeV, in the injector.

Due to these tradeoffs, hardly any dispute exists within the FEL community that the key development required to scale from the current kilowatt level to the baseline megawatt level is the high current injector. Additional research is required to ascertain the optimal energy of the injector.

Injector options include a photocathode gun with DC acceleration, a photocathode gun with RF acceleration at room, cryogenic, or superconducting temperatures, or a CW thermionic injector with RF acceleration. A trade study is required to assess the relative merits of DC guns and RF guns for high-average-power IR FEL's against consistent standards, and thereby, identify the break points, such as bunch charge, between the technologies. In general, RF guns may have an advantage in terms of beam quality at a higher bunch charge [Ref. 6].

Presently, the Jefferson Laboratory kilowatt FEL uses a photocathode injector with a 350 kV DC (electrostatic) accelerator. It provides about 5 mA average current in 60 - 110 pC bunches [Ref. 7]. The DC-gun performance is still probably sufficient for IRFEL purposes up to 1 nC, but it is roughly a factor 3 worse than could be achieved with a RF gun [Ref. 8].

2. Accelerator

In a linear accelerator, the bunches of electrons are accelerated to near the speed of light (relativistic velocities) using intense electric fields. The energy acquired by electrons in an accelerator is measured in electron volts (eV) which is the energy gained by an electron when it passes through an electric potential of 1 volt.

When an electron is accelerated to near the speed of light, its kinetic energy is $KE = (\gamma - 1)mc^2$ where the Lorentz factor is $\gamma = (1 - \mathbf{u}^2 / c^2)^{-1/2}$, \mathbf{u} is the electron speed, c is the speed of light in a vacuum, and mc^2 is its rest mass of about 0.5 million electron-volts (MeV). Typical accelerators for FELs operate in the range of 20 MeV ($\gamma \sim 40$) to 500 MeV ($\gamma \sim 1000$) [Ref. 7].

The most common electron accelerator for the FEL is a radio frequency linear accelerator (RF linac) which uses standing RF waves in the cavities to establish the accelerating electric fields. RF sources for FELs generally operate between 500 MHz and 2 GHz at frequencies where high power tubes are commercially available. Electron bunches are injected into the accelerator at the RF frequency or at a subharmonic, such as every 10th cycle.

The physical length of the accelerator is determined by the desired total acceleration (perhaps 100 MeV) and the achievable acceleration gradient, e.g., 6 MeV/meter, of the particular accelerator. A goal of the accelerator community has always been to increase the accelerator gradient, and thereby allowing for more compact devices.

Higher gradients are generally achievable using higher frequencies, while the size of the structure is also decreased. In addition, a higher RF frequency in the accelerating cavities is preferred because it enables one to keep the bunch charge smaller for a given average current and improve the beam quality [Ref. 9]. Roughly speaking, the beam degradation appears to be manageable for a sub-nC bunch charge, but becomes problematic at 1 nC where space charge effects degrade the beam unacceptably.

However, the accelerating cavities store more energy and have reduced wall interactions with the electron beam at low frequencies. Lower frequency RF allows larger

cavities and improved engineering of water channels able to dissipate heat generated by ohmic losses from the RF energy more efficiently. This permits higher average currents and peak charges with less degradation of beam quality than can be achieved with the higher gradients associated with the high frequency cavities. The optimal frequency is unknown, but appears to be somewhere around 750 MHz for this MW design [Refs. 8 and 10].

An alternative accelerator design uses superconducting RF technology that leads to a reduction of many orders of magnitude in resistive heating at the expense of adding cryogenic refrigeration. Jefferson Laboratory has demonstrated an FEL which produced 2.1 kW of average power using a superconducting RF Linac to produce a continuous stream of micropulses [Ref. 8].

Superconducting radio frequency (SRF) accelerators with energy recovery are the appropriate approach in a system where the added complexity is offset by the need for long run-times at moderate to high average power and where system efficiency is important. Analysis of the specific mission application and candidate accelerator designs would be required to determine whether a room temperature or superconducting accelerator is the best choice.

Over the past five years, SRF accelerators gradients have increased by more than a factor of two to ~ 10 MV/m, with 20 MV/m considered within near-term reach [Ref. 8]. Recent experiments have demonstrated greater than 1 kA peak current for high gain in amplifier systems with bunches of ~ 1 nC which are ~ 1 psec long.

3. Wiggler

The FEL's optical field is formed and amplified by the interaction of the relativistic electron beam with the spatially periodic magnetic field of the wiggler (Figure 2.2). Alternating the polarity of the magnets produces the desired magnetic field. This field's strength can be adjusted by varying the gap between the fixed magnet poles or by varying the current through electromagnets.

The wiggler's period, I_o , is the distance along the beam axis between magnet pairs. Wigglers are characterized by a dimensionless parameter $K = (eBI_o/2\beta mc^2) =$

$9.34BI_o$ where B is the rms magnetic field in kilogauss over each period and I_o is the wiggler period in centimeters. W wigglers are typically operated with $K \approx 1$ [Ref. 11].

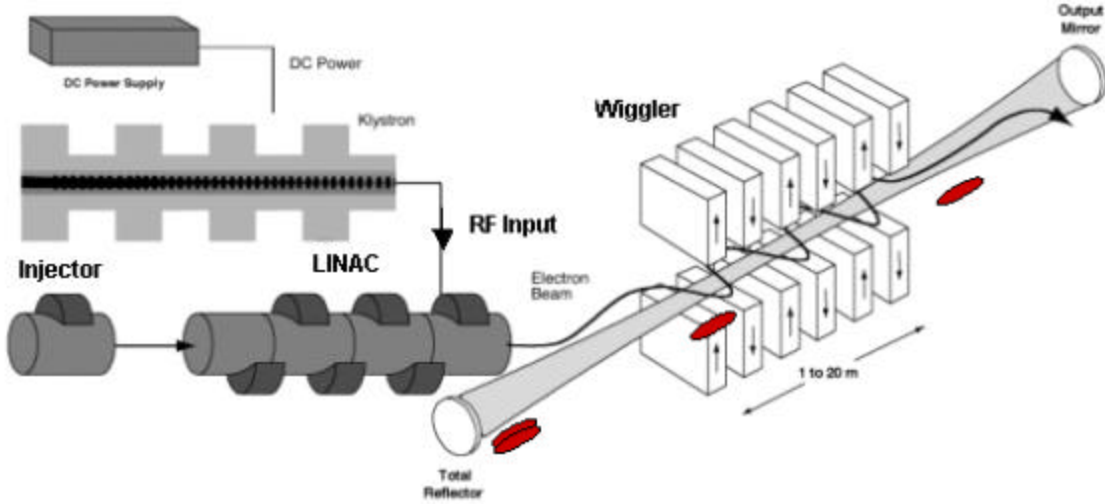


Figure 2.2. FEL Critical Components. (From [Ref. 1])

The FEL's output wavelength is given by $\lambda = (I_o/2g^2)(1 + K^2)$. From this equation, it can be seen that adjusting the wiggler period, the wiggler strength, or the electron beam's energy can change the wavelength of the FEL. For operation at wavelengths in the near infrared (IR) or less, required beam energies are in excess of 10 MeV [Ref. 9]. For instance, if $K = 1$, $I_o = 3$ cm, and the desired wavelength is $\lambda = 1 \mu\text{m}$, then the required energy is given by

$$g = \sqrt{\frac{I_o}{\lambda}} = \sqrt{\frac{3 \text{ cm}}{1 \mu\text{m}}} \approx 170 \Rightarrow E_{beam} \approx 85 \text{ MeV} \quad (2.2)$$

FELs also require electron beams with low emittance (small radius and angular spread) and very small energy spread (highly monoenergetic) [Ref. 7]. As the electron beam passes through the wiggler, only a small fraction of its kinetic energy is converted to optical energy. As energy is extracted, the electron beam bunches longitudinally and the energy spread increases. If the FEL uses energy recovery, only minor degradation of the electron beam is tolerable. For recirculating FELs no more than a few percent of the beam energy can be extracted and converted into optical energy each pass. If, however,

the remaining beam is to be discarded (as in a regenerative amplifier), then much more of the beam energy might be extracted. This is usually achieved by tapering the wiggler period or magnetic field strength to maintain the resonance condition as the electron beam loses its kinetic energy to the light wave.

4. Resonator

In an oscillator FEL, the optical cavity is oriented along the wiggler axis and extends beyond the wiggler length, bounded by the resonator optics as in a conventional laser (Figure 2.2). During successive passes of the optical pulses through the wiggler, the optical beam is amplified and a fraction of the coherent radiation is allowed to escape and become the outcoupled optical energy from the FEL.

For maximum coupling efficiency, the optical beam within the resonator must roughly match the electron beam size [Ref. 11]. This is quite small within the wiggler, ranging from 100 μm to a millimeter in diameter [Ref. 7]. As a result, the laser beam is very small and intense when it strikes the resonator optics. This problem is exacerbated by increasing the FEL's average power. If resonator length is not a design constraint, this problem can be helped by separating the mirrors widely and allowing diffraction to spread the optical beam. For compact applications, i.e., to meet shipboard packaging requirements, this is not an option and alternate resonator concepts, such as a short Rayleigh length design or higher damage threshold optics, must be developed.

C. MW-CLASS FEL PROPOSED DESIGN

The FEL design that seems to be the most attractive for a MW class FEL weapon system is shown in Figure 2.3. The electron beam is created in a SRF photoinjector, which then introduces the beam into a recirculating loop consisting of an SRF accelerator and a cryo-cooled sapphire mirror oscillator connected by bending magnets. The high-energy-acceptance bends manipulate the beam phase space to preserve beam quality prior to reinsertion 180 degrees out-of-RF phase into the SRF accelerator. The electron beam is then decelerated and delivered to the beam dump at low energy. This key aspect of same-cell energy recovery, already convincingly demonstrated by the Jefferson Laboratory IR FEL, leads to high wall-plug efficiency and minimizes the radiation and shielding requirements for the laser [Ref. 8]. MW-class FELs are projected to be 10-20% wall-plug efficient.

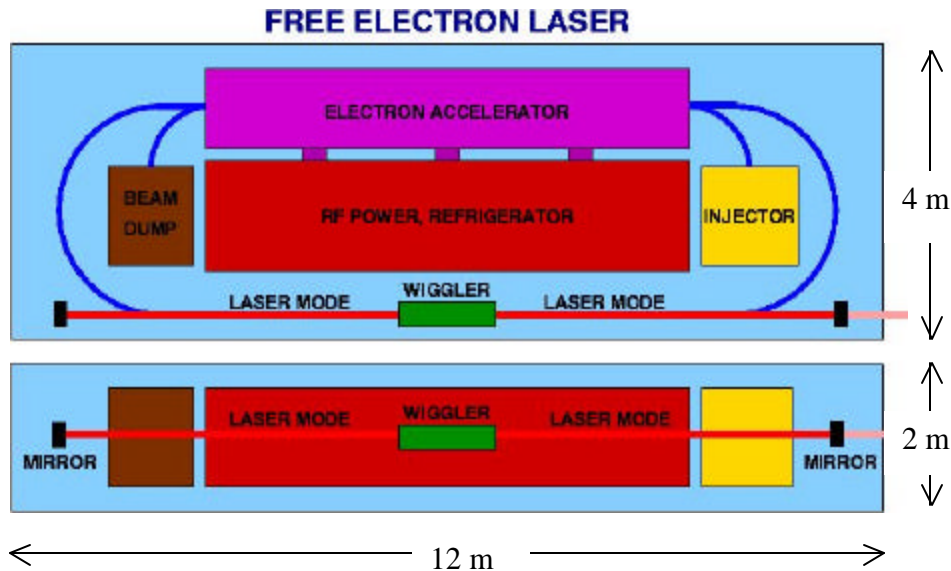


Figure 2.3. Schematic Diagram of a MW Level FEL Weapon System. (From [Ref. 12])

FEL technology has made great strides in the past five years with the recent demonstration of 2.1 kW at Jefferson Laboratory. FELs are now in the same regime as state-of-the-art solid-state lasers and, may in fact, be scalable to much higher powers.

D. SSL DESIGN

The typical structure of a Solid-State-Laser (SSL), which is similar to other conventional lasers, is shown in Figure 2.4. The flash lamp pump inverts the electron population in the lasing material (rod), leading to energy storage in an upper atomic level. If this energy is released to the optical beam by stimulated emission, or the downward transition under the presence of light, amplification takes place. After spontaneous radiation (downward transition independent of the presence of light) is emitted along the axis of the laser, the system starts to oscillate if the feedback determined by the reflectivity of the mirrors is sufficiently large. The role of the resonator (optical cavity) is to maintain an optical mode whose losses are replenished by the amplifying medium through stimulated emission.

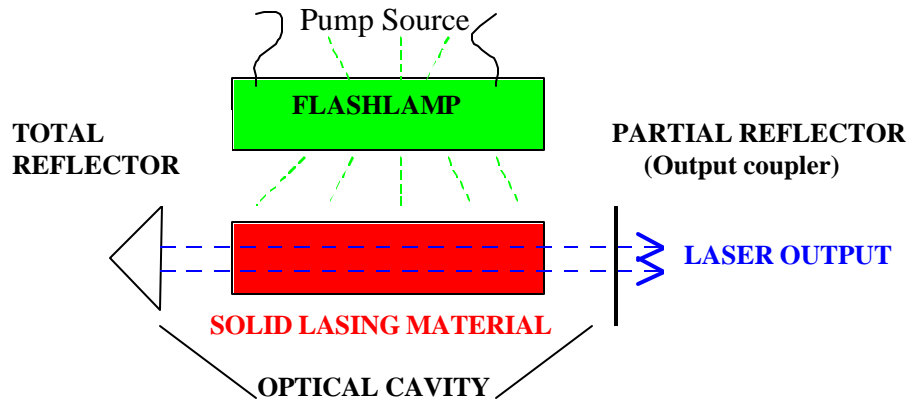


Figure 2.4. Elements of a Typical Solid State Laser.

A considerable amount of progress has been made over the last 15 years in scaling solid-state lasers to higher powers. Kilowatt average power levels are now routine, and 10 kW output, it is believed, will soon be demonstrated. Systems at the 100 kW level are being designed today, and conceptual designs for MW-level devices have been developed by multiple industrial sources.

However, vastly increasing technology efforts are focusing on three keys to high energy [Ref. 6]:

- design and manufacturing of reliable diode pump lasers
- phased combining of laser modules
- thermal control of laser media

E. CHALLENGES FOR MW-CLASS SSL

1. Laser Diodes

Among the various light sources that have been employed over the years to pump solid-state lasers, the diode lasers are most promising for pumping high energy SSLs. The most basic form of a diode laser consists of a semiconductor in which one part is doped with electron donors to produce n-type material and the other part is doped with electron acceptors (holes) to produce p-type material. Application of forward bias in this p-n junction drives electron and holes into the junction region where electron-hole recombination takes place, releasing energy in the form of photons [Ref. 13].

Some of the major attributes of diode pumping are high pumping efficiency, improved beam quality due to the spectral match between the laser diode-laser emission

and the absorption band of the laser material, increased lifetime, directionality and a small emitting area of the diode output [Ref. 14].

However, laser diodes, as with all semiconductors, are devices very sensitive to temperature. Thus, the need to maintain the operating temperature within a relative narrow range requires a more elaborate thermal management system when compared to flashlamp pumped lasers.

Diode arrays, arrays containing a number of stripe lasers on a single chip, have demonstrated more than 1 kW/cm^2 output intensity [Ref. 6]. However, pumping HELs, designs which produce higher coherence, require high intensity pumping ($> 10 \text{ kW/cm}^2$) and thermal management is one of the principle challenges to achieving higher power diode arrays. Present diode arrays operate efficiently at junction temperatures up to $50\text{--}60^\circ\text{C}$. Operation at up to $\sim 100^\circ\text{C}$ has been demonstrated, but at decreased efficiency and lifetime.

The peak power of the diodes also determines their packaging and cost. A typical engagement requires $\sim 1 \text{ MJ}$ of energy to the beam director, e.g., 400 kW output for 2.5 sec . Since the laser medium itself will be only about 40% efficient, 2.5 MJ of diode energy must be delivered to the laser head. This corresponds to an average diode pump array power of $\sim 1 \text{ MW}$ delivered during the engagement burst. A pulsed mode operation of the diodes with 10% duty cycle would then require a peak power capability of 10 MW .

Present cost is in the range of $\$10$ per peak-Watt for pulsed arrays, $\$30$ per W for CW arrays, and is dominated by the cost of the coolers. Lawrence Livermore National Laboratory (LLNL), Navy-Mantech, and Air Force Research Laboratory (AFRL) all have programs to reduce the cost and improve the reliability of diode pump arrays for high-energy lasers.

2. Phasing of Laser Modules (Fiber Lasers)

Another promising method to scale SSLs to high energy is to phase the laser modules. The “phase-locking” technology is an active research area in industrial, DOD, and DOE laboratories. Phase locking works towards coherently combining multiple laser modules. The Phase Integrated Laser Optics Technology (PILOT) program, conducted at

AFRL during the late 1980s and early 1990s, demonstrated coherent phasing of 900 low power diode elements with total output power ~ 10 Watts.

Similar phasing techniques may be applied to current fiber lasers efforts to produce high-power fiber module devices. Current state-of-the-art fiber lasers produce diffraction-limited output but are limited in power to approximately 100 W [Ref. 6].

In principle, combining one thousand fibers, each operating at 100 W would produce a 100 kW laser system from an aperture less than 1 cm^2 in area. The problem is that each individual fiber is an independent laser. As a result, the output of the individual fibers adds incoherently and the overall divergence of the fiber array is the same as for any one fiber. In other words, the array indeed produces 100 kW output power but in a highly divergent beam with a time-dependent, random coherence.

If the technology to coherently couple the output of individual fibers, or the phase-locking of one fiber to another, can be developed then the promise of high power fiber lasers can be realized. The state-of-the-art laser is the achievement of two low power fibers successfully phase-locked together producing a coherent output of ~ 100 mW [Ref. 6].

3. Thermal Control of Laser Media

Thermal management is essential to solid-state laser operation since the increase in temperature distorts the lasing medium. The temperature gradients degrade beam quality and possibly deplete the laser gain by thermally exciting the lower atomic level. Both of these effects degrade the utility of solid-state lasers as weapons. Degradation of beam quality limits the achievable irradiance on target, while excitation of the lower atomic level limits the amount of laser energy and/or duration of the laser burst. Efficient heat removal usually dominates designs for high-average-power systems.

The cooling techniques are described in Ref. 14. In most laser architectures, removal of the thermal load is accomplished by conduction through the laser material (convection on the surface) [Refs. 14 and 14]. The term *continuously cooled lasers* is used to refer to lasers where excitation and cooling of the laser medium occur simultaneously. These lasers have the longest history of achieving kilowatt-level output power.

However, the combination of volumetric heating of the laser material by the absorbed pump radiation and surface cooling required for heat extraction results in temperature gradients across the active area. This creates thermal lensing effects, due to a temperature-dependent variation of the index of refraction, which significantly degrades the laser's beam quality.

An additional issue associated with thermal loading is stress fracture of the laser material. Stress fracture occurs when the stress induced by temperature gradients in the laser material exceeds the tensile strength of the material.

An incremental improvement to these effects can be achieved by using a “Slab laser with Zig-Zag optical path” (Figure 2.5). The rectangular-slab laser provides a larger cooling surface and essentially a one-dimensional temperature gradient across the thickness of the slab. Additionally in the zig-zag geometry, the optical beam does not travel parallel to the z axis. Instead the beam traverses the slab at an angle with respect to the x - z plane using total internal reflection from the slab y faces. Since the thermal profile is symmetrical relative to the center plane of the slab, the thermal stress averaged from one slab surface to the other (in the ideal case) is zero. However, despite the elegance of this design the performance of these systems has been noticeable poorer than predicted.

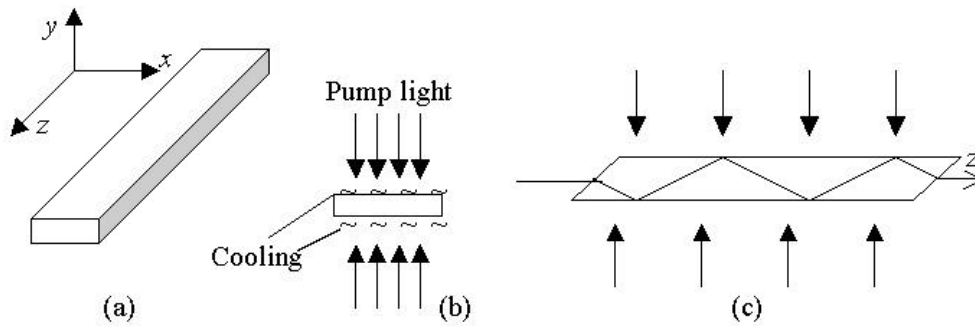


Figure 2.5. Schematic of a zig-zag slab Laser. (a) Slab geometry, (b) End view, (c) Optical path in y - z plane. (After [Ref. 14])

Diode-pumped Neodymium-doped Lasers (Nd:YAG, Nd:YLF, and Nd:YVO₄) originally dominated this class of lasers. Scaling to higher average power with continuously-cooled Nd-doped lasers may be difficult due to the relatively large quantum defect associated with Neodymium as explained in the next chapter. A possible approach

to achieving higher average power output from continuously cooled lasers is by using other materials, such as Ytterbium (Yb), in place of Nd, with lower quantum defect and require substantially less cooling and produce a better beam quality than a Nd:YAG device.

F. HEAT CAPACITY LASER

Of all the solid-state laser concepts, probably the closest to achieving 100 kW level output power is the *heat capacity laser*, which will be discussed in detail [Ref 6]. The heat capacity laser name is derived because lasing and cooling occur separately. See Figure 2.6. A pulse sequence begins by switching electrical current through the diode arrays, which excites the laser diodes and produces pump light for the laser crystals. As energy is absorbed within the crystals, the laser gain increases until it exceeds the cavity loss. At this point, lasing occurs within the cavity in free running mode. During the lasing cycle, pump radiation is continuously absorbed, while, simultaneously, heat is deposited in the laser crystal by the residual energy left behind. This energy is dominated by the quantum defect, which is equal to the difference in energy between the photons absorbed and those emitted (~ 0.36 eV for Nd lasers).

The crystal temperature increases linearly throughout the lasing cycle. Laser emission is terminated by the user when target kill achieved, or when the lower atomic level becomes thermally populated, or when thermally-induced cavity losses exceed the available gain. At this point, current to the diode pump arrays is halted and a cool-down cycle begins.

The amount of heat that can be deposited in the medium before lasing ceases is determined by the medium's heat capacity. Since it is the total heat deposited which limits total operation time, heat capacity lasers are often referred to as having a "thermal magazine." The thermal magazine may correspond to several target kills. Once the crystal has reached its heat capacity limit, it must be cooled before another cycle begins.

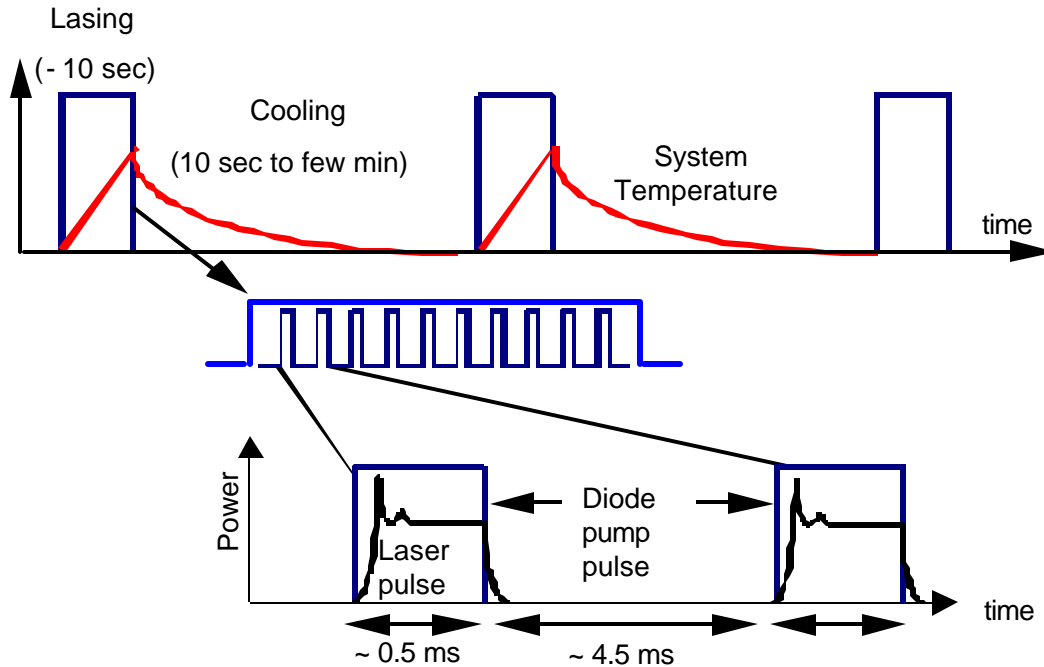


Figure 2.6. Heat Capacity Laser Concept. (From [Ref. 6])

The HCL laser module envisioned for the Army's Enhanced Area Air Defense (EAAD) mission can operate for ~ 10 seconds before reaching its heat capacity limit. Since each engagement could last between 2 and 3 seconds, a total of ~4 target engagements could be achieved before the laser has to initiate a cool-down cycle. Depending upon the cooling technology, a cool-down cycle of 0.5 to 5 minutes would be required before the system is fully reset to room temperature.

A state-of-the-art heat capacity laser has been recently completed that is flashlamp-pumped and reaches 10 kW. It has 500 J per pulse at 20 Hz pulse repetition frequency operated at LLNL. See Figure 2.7. While only 1.4 kW (140 J at 10 Hz) average power has been demonstrated to date, the laser has recently exceeded the pulse energy design goal significantly by operating in a single-shot mode at over 1000 J per pulse. Replacing the flashlamp pump sources with diode lasers and replacing the Nd:glass laser disks with Neodymium-doped Gadolinium Gallium Garnet (Nd:GGG) crystals, is expected to improve a power-scaled version of this laser to achieve more than 100 kW (500 J pulses at > 200 Hz repetition rate).

The High Energy Laser Systems Test Facility (HELSTF) received the 10 kW devices in August 2001 for integration into a testbed. Static tests are currently being conducted to evaluate and characterize the device in support of developmental testing that will lead to the 100 kW SSHCL prototype.

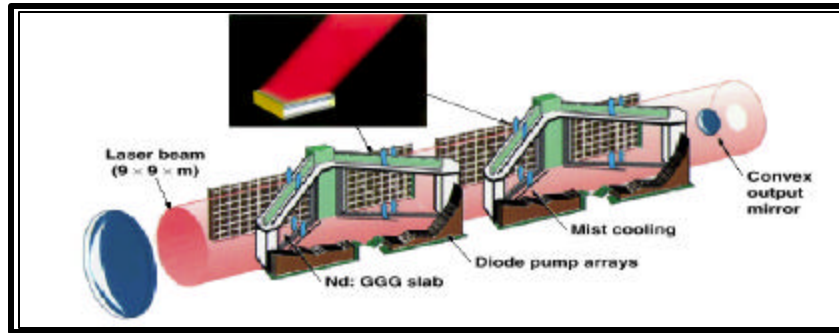


Figure 2.7. LLNL 100 kW SSHCL Design. (From [Ref. 1])

There is a detailed Army/LLNL development plan for the 100 kW HCL demonstrator. See Figure 2.8. This plan is comprehensive in that it addresses most of the subsystems that will be required to achieve a viable heat capacity laser: diode arrays, laser crystal availability, and power supplies. Perhaps the most significant issue with heat capacity lasers that is not currently being addressed is cooling the active medium between lasing cycles. LLNL has suggested both gas (convective) and evaporative “mist” cooling. Little work has been done in this area, and it is unclear how these cooling methods will perform, including their impact on system complexity. However, the cool-down cycle is a critical factor that directly affects the reset time between magazines and may impose limits on the operational capabilities.

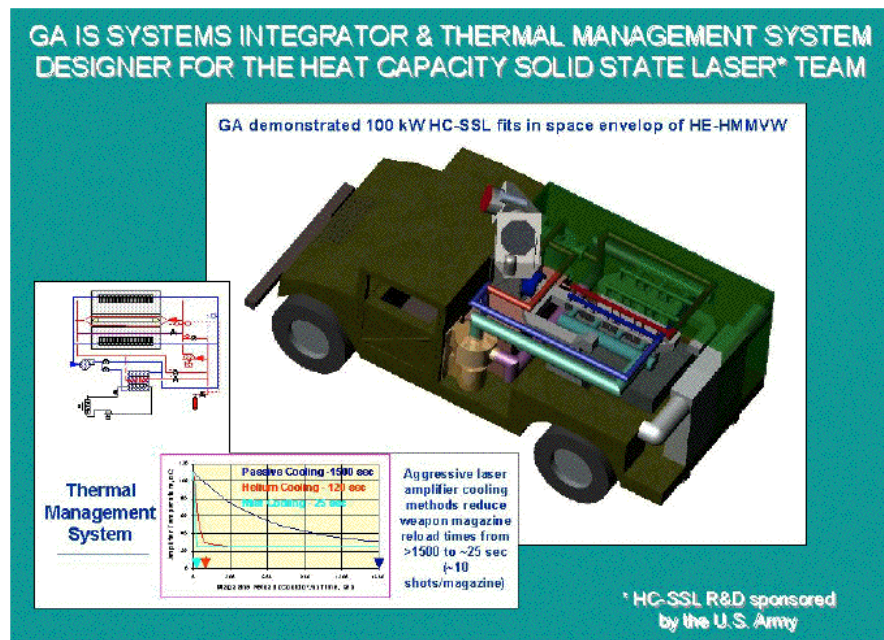


Figure 2.8. SSHCL 100 kW Demonstration Concept for the Army. (From [Ref. 3])

G. CONCLUSIONS

This chapter discussed the recent HEL science and technology developments for both FELs and SSLs. Areas needing improvements were addressed.

In general, FELs can produce powerful, high coherent, optical beams but also place extreme demands on the resonator mirrors while SSLs in general produce a larger beam spot and thus subjects optics to lower a damage threshold. They do not, however, achieve the desirable beam quality. Efficient heat removal from the laser media is needed in high-power SSL designs, while high-power FELs require high-brightness injectors and novel optical cavity designs. However, considering the vastly increasing research development efforts, both technologies have the potential to meet the needs of a weapon-class laser.

Fiber optic lasers and the Heat Capacity Laser project are examples of the readiness of solid-state laser technology for rapid maturation. On the other hand, the unique advantages of FELs, such as wavelength selectability and tunability, high beam quality, the potential to achieve high peak power without distorting the lasing media and long run-time, could favor FELs for weapon-class lasers in the near future.

III. PHYSICS OF SOLID-STATE AND FREE ELECTRON LASER

The word 'LASER' is an acronym standing for 'Light Amplification by Stimulated Emission of Radiation'. The output of a laser can be infrared, visible, or ultraviolet radiation in a pulsed or a continuous beam, with average power from less than a milliwatt to several megawatts of power. However, all conventional lasers have the following in common:

- a lasing medium which can be a solid, liquid, or gas,
- a means of pumping energy (optical, electrical, mechanical or chemical) into the lasing medium.

In a Solid-State Laser (SSL), the active medium is a solid material and optical energy is used as an external pump source. The Free Electron Laser (FEL) represents a radical alternative to all conventional lasers where the active medium is a relativistic electron beam. This chapter will outline the basic ideas underlying the operation of both types of lasers.

A. PHYSICS BEHIND SOLID STATE LASERS

To understand the operation of a SSL, which is actually similar to all conventional lasers, it is necessary to know some of the principles governing the interaction of radiation with matter. Many of the properties of lasers may be readily discussed in terms of the absorption and emission processes, which take place when an atomic system interacts with a radiation field. Einstein's discovery of stimulated emission provided essentially all of the theory necessary to describe the physical principle of the laser.

1. Einstein A and B Coefficients

Consider an idealized material consisting of atoms with just two nondegenerate energy levels, E_1 and E_2 , having populations of N_1 and N_2 , respectively. Of particular interest is the interaction between an atom and a photon of frequency $f = f_{21}$, such as $hf_{21} = E_2 - E_1$ where h is Planck's constant. Three types of interactions can be identified: absorption, spontaneous emission and stimulated emission.

a. Absorption

An atom in state 1 absorbs a photon from the radiative field and thus converts the atom into state 2. The rate at which this process takes place depends on the

concentration of absorbing atoms and the intensity of the field from which they extract the energy, as is expressed by

$$\left(\frac{\partial N_2}{\partial t} \right)_{abs} = +B_{12} \mathbf{r}_s(f) N_1, \quad (3.1)$$

where B_{12} is a constant of proportionality and $\mathbf{r}_s(f)$ is the radiation density.

b. Spontaneous Emission

After an atom has been raised to the upper level 2 by absorption, the population of the upper level 2 decays spontaneously to the lower level at a rate proportional to the upper level population, as expressed by

$$\left(\frac{\partial N_2}{\partial t} \right)_{spont} = -A_{21} N_2, \quad (3.2)$$

where A_{21} is a constant of proportionality and called the spontaneous transition probability (the probability that an atom in level 2 will spontaneously change to a lower level 1 within a unit of time). The reciprocal of transition probability of a process is called its lifetime,

$$t_{21} = A_{21}^{-1}. \quad (3.3)$$

Spontaneous emission is a statistical function of space and time, and there is no relation between the individual emission processes; the photons emitted incoherently.

c. Stimulated Emission

Emission takes place, not only spontaneously but also under stimulation by electromagnetic radiation of the same frequency. This process is the reverse of absorption. The atom gives up its excess energy hf to the field, adding coherently to the intensity. Thus, the added photon is at the same frequency, at the same phase, in the same sense of polarization, and propagates in the same direction as the photon that induced the atom to undergo this type of transition. The rate depends on the density of atoms to be stimulated and the intensity of the stimulating field.

$$\left(\frac{\partial N_2}{\partial t} \right)_{stim} = -B_{21} \mathbf{r}_s(f) N_2, \quad (3.4)$$

where B_{21} again is a constant of proportionality.

If we combine absorption, spontaneous, and stimulation emission as expressed by (3.1), (3.2) and (3.4) we can write for the change of the upper and lower level populations

$$\frac{\partial N_2}{\partial t} = -A_{21}N_2 + B_{12}\mathbf{r}_s(f)N_1 - B_{21}\mathbf{r}_s(f)N_2 = -\frac{\partial N_1}{\partial t}. \quad (3.5)$$

At thermal equilibrium, the time rate of change must be zero. Therefore

$$A_{21}N_2 + B_{21}\mathbf{r}_s(f)N_2 = B_{12}\mathbf{r}_s(f)N_1. \quad (3.6)$$

Using the Boltzmann equation and the Plank formula for the black body radiation law, the following relations between A 's and B 's which are known as Einstein's relations are obtained [Ref. 16],

$$\frac{A_{21}}{B_{21}} = \frac{8\pi f_{21}^3 h}{c_s^3} \text{ and } B_{21} = \frac{g_1 B_{12}}{g_2}, \quad (3.7)$$

where g_1, g_2 are the degeneracies of levels 1 and 2 respectively, $c_s = c/n$ is the speed of light in the laser medium, n is the index of refraction and c is the speed of light in vacuum.

2. Atomic Lineshapes

In deriving Einstein's coefficients, a monochromatic wave with frequency f_{21} acting on a two-level system with an infinitely sharp energy gap hf_{21} has been assumed. The interaction between an atomic system having a finite transition linewidth Δf and a signal with a bandwidth df will now be considered. The result is that a distribution of photon frequencies $g(f)$ can be emitted (or absorbed). This relative distribution is called the lineshape function, with $g(f)df$ being the probability that a given transition will result in an emission or absorption of a photon with energy between hf and $h(f+df)$.

The linewidth and lineshape of an atomic transition depends on the cause of line broadening. Optical frequency transitions in solids can be broadened by lifetime, dipolar or thermal broadening, or by random inhomogeneities. Two generic types of processes contribute to the width of a spectral line.

a. The Homogeneous Broadened Line

The essential feature of a homogeneously broadened atomic transition is that every atom has the same atomic lineshape and frequency response, so that a signal applied to the transition has exactly the same effects on all atoms in the collection. Mechanisms that result in a homogeneously broadened line are lifetime broadening, collision broadening, dipolar broadening and thermal broadening. The lineshape of homogeneously broadening mechanisms leads to a Lorentzian lineshape for atomic responses [Ref. 17] as expressed by

$$g(f) = \left(\frac{\Delta f}{2p} \right) \left[(f - f_o)^2 + \left(\frac{\Delta f}{2} \right)^2 \right]^{-1}, \quad (3.8)$$

where f_o is the center frequency, and Δf is the full-width half-maximum of the power spectrum. The factor $\Delta f/2p$ assures normalization of the area under the curve.

b. The Inhomogeneous Broadened Line

Mechanisms, which cause inhomogeneous broadening, tend to displace the center frequencies of individual atoms, thereby broadening the overall response of a collection without broadening the response of individual atoms. Different atoms have slightly different resonance frequencies at the same transition. As a result, the over-all response of the collection is broadened. Examples of inhomogeneous frequency-shifting mechanisms include Doppler broadening and broadening due to crystal inhomogeneities. The inhomogeneous-broadened linewidth can be represented by a Gaussian frequency distribution [Ref. 17]

$$g(f) = \frac{2}{\Delta f} \left(\frac{\ln 2}{p} \right)^{1/2} \exp \left[- \left(\frac{f - f_o}{\Delta f / 2} \right)^2 \ln 2 \right]. \quad (3.9)$$

3. Amplification in a Laser

The interaction between two linewidth-broadened energy levels with an energy separation centered at f_o , and a half width of Δf characterized by $g(f)$ and a narrow band signal with bandwidth $df \ll \Delta f$ will be considered next. Equation (3.5) then becomes

$$\frac{\partial N_2}{\partial t} = -A_{21}N_2 + B_{12}\mathbf{r}_s g(f)N_1 - B_{21}\mathbf{r}_s g(f)N_2. \quad (3.10)$$

Using (3.7)

$$\frac{\partial N_2}{\partial t} = -A_{21}N_2 - \left[N_2 - \frac{g_2}{g_1} N_1 \right] \frac{I_f}{hf} \mathbf{s}(f), \quad (3.11)$$

where $I_f = c\mathbf{r}_s/n$ represents the intensity of the radiating field, \mathbf{r}_s is the radiation density of the field and $\mathbf{s}(f) = A_{21}g(f)\mathbf{I}^2/8\mathbf{p}n^2$ is the cross-section area of the beam.

Since each transition carries energy hf and $\partial N_2/\partial t$ represents the transition rate, we have

$$-hf \frac{dN_2}{dt} = \frac{dI_f}{dz}, \quad (3.12)$$

where z is the direction the beam travels.

Combining Equations (3.11) with (3.12) and neglecting the spontaneous emission we get

$$I_f = I_o e^{\left(N_2 - \frac{g_2}{g_1} N_1 \right) \mathbf{s}(f) z}, \quad (3.13)$$

which can also be written as

$$I_f = I_o e^{\mathbf{g}_o(f) z}, \quad (3.14)$$

where

$$\mathbf{g}_o(f) = \mathbf{s}(f) \left(N_2 - \frac{g_2}{g_1} N_1 \right) = A_{21} \frac{\mathbf{I}^2}{8\mathbf{p}n^2} g(f) \left(N_2 - \frac{g_2}{g_1} N_1 \right) \quad (3.15)$$

is known as the laser gain equation. From Equation 3.15, it is obvious that, in order to have gain, it is necessary to have $N_2 > (g_2/g_1) N_1$ and for $g_2 = g_1$, $N_2 > N_1$.

According to the Boltzmann distribution, in a collection of atoms at thermal equilibrium, there are always fewer atoms in a higher-energy level E_2 than in a lower level E_1 . Therefore, the population difference $N_1 - N_2$ is always positive and gain does not occur. The situation $N_2 > N_1$, which is required for a laser operation, is called population inversion and is never observed at thermal equilibrium.

4. Population Inversion

This section is concerned with how the necessary population inversion for laser gain is obtained in solid-state lasers. Considerable understanding can be gleaned on how laser devices are pumped and how their population densities are inverted by studying some simplified but fairly realistic models.

The discussion until now has been based on a hypothetical two-level system. The pumping and laser processes in real laser systems typically involve a very large number of energy levels. The main feature can be understood, however, through the familiar three-level or four level idealizations of Figures 3.1 and 3.2.

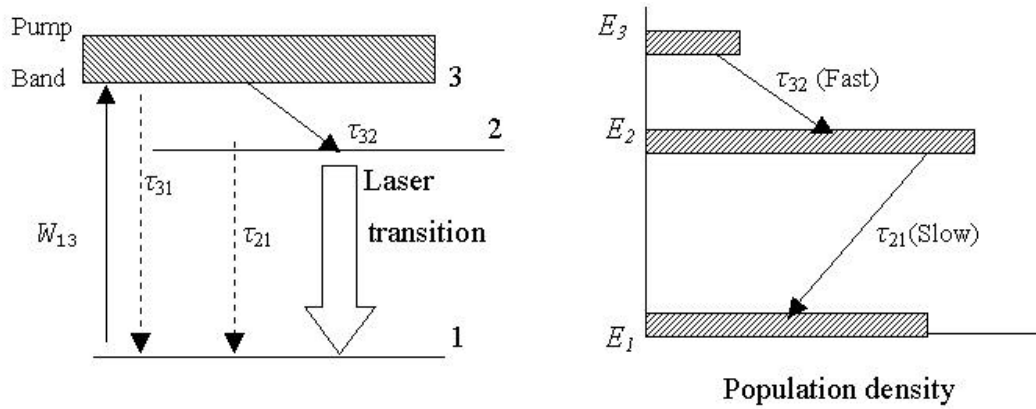


Figure 3.1. Simplified Energy Diagram of a Three-Level Laser. (From [Ref. 14])

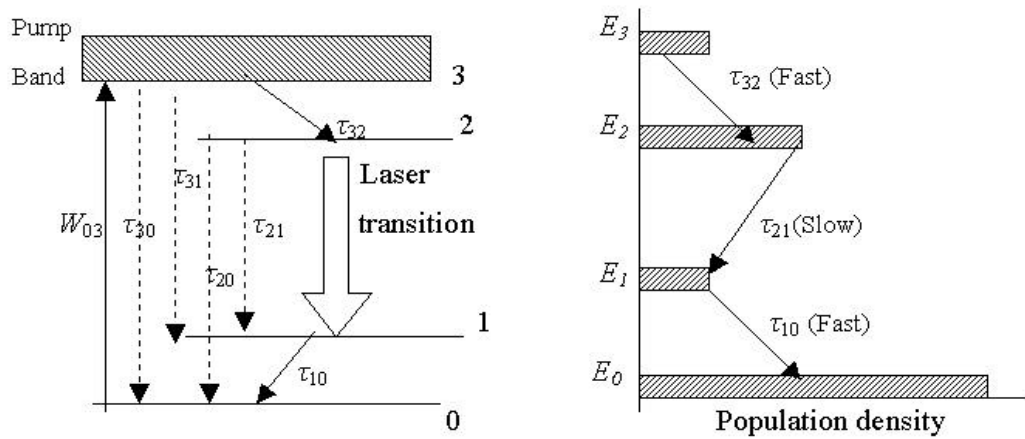


Figure 3.2. Simplified Energy Diagram of a Four-Level Laser. (From [Ref. 14])

a. *The Three-Level System*

In a three-level laser, most of the atoms of the laser material are initially in the lowest level 1 (ground state). Excitation is supplied to the medium by the radiation pump source producing absorption into the broad band 3. Most of the excited atoms are transferred by fast, radiationless transitions into the intermediate sharp level 2. In this process, the energy lost by the electron is transferred to the lattice. The difference between these two levels $E_3 - E_2$ is known as “quantum defect” and represents the laser’s minimum possible heat load. Finally, the electrons return to the ground level by the emission of a photon. It is this last transition that is responsible for the laser action.

The basic disadvantage of a three-level system is that more than half of the atoms in the large-populated ground state must be raised to the metastable level E_2 in order to create inversion, which requires strong pumping.

b. *The Four-Level System*

The four-level system is characteristic of the rare earth ions in glass or crystalline host materials. The pump transition extends again from the ground state, now level E_0 to a wide absorption band E_3 . As in the three-level system, the atoms will proceed rapidly to the sharply defined level E_2 . The laser transition, however, proceeds now to a fourth, terminal level E_1 that is situated above the ground state E_0 . From here, the atom undergoes a rapid nonradiative transition to the ground level. In a four-level system, an inversion of the $2 \rightarrow 1$ transition can occur even with vanishingly small pump power so the high pump rate necessary in the three-level system is no longer needed.

After this brief description of the energy levels, it is now obvious that the metastable level is of paramount importance for laser action to occur. The relatively long lifetime of the metastable level provides a mechanism by which the inverted population can be achieved. Most transitions of atoms show rapid nonradiative decay since the coupling of the internal atomic oscillations to the surrounding lattice is strong. In typical laser systems with energy levels, such as those shown in Figures 3.1 and 3.2, the $3 \rightarrow 2$ and $1 \rightarrow 0$ transition frequencies fall within the frequency range of the vibration spectrum of the host crystal lattice. Therefore, all these transitions can relax extremely rapidly by

direct nonradiative decay, emitting a phonon to the lattice vibrations, with lifetimes like $t_{32}, t_{10} \approx 10^{-8}$ to 10^{-11} s. However, the larger $3 \rightarrow 0$, $3 \rightarrow 1$, $2 \rightarrow 0$, and $2 \rightarrow 1$ energy gaps often correspond to frequencies that are higher than the highest possible vibration frequency of the lattice. These transitions must then occur either by radiative (photon) emission or by multiple phonon processes. Since both these processes are relatively weak compared to direct single-phonon relaxation, the high frequency transitions will have much slower relaxation rates ($t_{21} \approx 10^{-5}$ to 10^{-3} s). Therefore, the various levels lumped into level 3 will all relax mostly into level 2. Level 2 is metastable (long-lived) since there are no other levels located close below it into which the atoms can be decayed directly. In order for the population inversion to increase, it is also required that $t_{30} \gg t_{32}$ and $t_{21} \gg t_{10}$.

To achieve the correct combination of relaxation times and the existence of broad pump bands, a suitable material must be used.

5. Solid-State Laser Materials

Materials for laser operation must possess sharp fluorescent lines, strong absorption bands, and a reasonable high quantum efficiency for the transition of interest. These characteristics are generally shown by solids (crystals or glass) which incorporate in small amounts of elements in which optical transitions can occur between states of inner, incomplete electron shells. The two principal elements of a solid-state laser medium are the host materials and the activator/sensitizer ions.

a. Host Materials

The host materials must have good optical, mechanical and thermal properties to withstand the severe operating conditions of practical lasers. Desirable properties include hardness, chemical inertness, the absence of internal strain and refractive index variations, and ease of fabrication. *Glasses* form an important class of host materials. The outstanding practical advantage compared to crystalline materials is the tremendous size capability for high-energy applications. The optical quality can be excellent, and beam angles approaching the diffraction limit can be achieved. Glass is easily fabricated and takes a good optical finish. Generally, the advantages of *crystalline* laser hosts over glass are their higher thermal conductivity, narrower fluorescence

linewidths and, in some cases, greater hardness. Some of the most useful laser hosts are the synthetic garnets: yttrium aluminum, $\text{Y}_3\text{Al}_5\text{O}_{12}$ (YAG), and gadolinium gallium garnet, $\text{Gd}_3\text{Ga}_5\text{O}_{12}$ (GGG). These garnets are hard, stable, optically isotropic, and have good thermal conductivities, which permits laser operation at high average power levels (SSHCL).

b. Active Ions

Among many others, the rare earth ions are natural candidates to serve as active ions in solid-state laser materials because they exhibit a wealth of sharp fluorescent transitions representing almost every region of the visible and near-infrared spectrum. Neodymium (Nd^{3+}) was the first of the trivalent rare earth ions to be used in a laser, and it remains by far the most important element in this group. Stimulated emission has been obtained with this ion incorporated in at least 100 different host materials and a higher power level has been obtained from Nd lasers than from any other four-level material. Other rare earth ions in which laser action has been reported are Erbium, Holmium, Thulium, Gadolinium, Europium and Ytterbium. Diode-pumped Yb: YAG has especially become an important laser because it produces, due to small quantum defect, the smallest amount of crystal heating compared to any other major laser system.

B. PHYSICS BEHIND FREE ELECTRON LASERS

The Free Electron Laser (FEL) is a different kind of laser, which uses a relativistic electron beam as the active medium moving along a periodic magnetic field. The electrons are not bound to atoms, but they are not truly free since the wiggler field governs their motion. The FEL requires that the electrons undergo periodic oscillations in the transverse plane while moving at nearly the velocity of light along the z direction. The periodic oscillation implies an acceleration, which causes the electrons to radiate (spontaneously) perpendicular to their wiggling motion (like an oscillating dipole). If the z component of velocity is large $u_z \sim c$ (a highly relativistic beam), the radiation pattern is primarily in the $+z$ direction and can be found from the relativistic Larmor formula [Ref. 11]. The spontaneous emission is stored in an optical cavity and amplified in succeeding passes by the relativistic electron beam (Figure 2.2). In order to understand how a relativistic electron can be coupled to the optical power, it is necessary to study the electron dynamics in the undulator.

1. Electron Motion

The easiest way to derive the electron trajectories is for the case of a relativistic beam interacting with a helical undulator, or a circular polarized array of magnets. Near the undulator axis, the magnetic field can be expressed as

$$\vec{B}_u = B(\cos(k_o z), \sin(k_o z), 0), \quad (3.16)$$

interacting with a circular polarized optical electromagnetic field given in cgs units by

$$\vec{E}_s = E(\cos(\mathbf{y}), -\sin(\mathbf{y}), 0), \quad (3.17)$$

$$\vec{B}_s = E(\sin(\mathbf{y}), \cos(\mathbf{y}), 0), \quad (3.18)$$

where B is the magnetic field of the undulator, E is optical field amplitude, $k_o = 2\pi/l_o$ is the wave number of the undulator, $\mathbf{y} = (kz - \omega t + \mathbf{f})$ is the phase of the optical wave, and \mathbf{f} is the initial optical phase at $t=0, z=0$.

The problem being faced is to solve the relativistic Lorentz force equations

$$\frac{d(\mathbf{g}mc\vec{\mathbf{b}})}{dt} = -e(\vec{E} + \vec{\mathbf{b}} \times \vec{B}), \quad (3.19)$$

$$\frac{d(\mathbf{g}mc)}{dt} = -e\vec{\mathbf{b}} \cdot \vec{E}, \quad (3.20)$$

where the Lorentz factor is

$$\mathbf{g} = \frac{1}{\sqrt{1 - \vec{\mathbf{b}} \cdot \vec{\mathbf{b}}}}, \quad (3.21)$$

$\vec{\mathbf{b}} = \vec{\mathbf{u}}/c$ is the dimensionless electron velocity, c is the speed of light, m is the rest mass of electron, e the electron charge magnitude and $\vec{B} = \vec{B}_s + \vec{B}_u$.

Integrating Equation (3.19) using the undulator field from Equation (3.16) and the optical field from Equations (3.17), (3.18), and ignoring terms proportional to $1 - \mathbf{b}_z$ for relativistic electrons, we get

$$\vec{\mathbf{b}}_{\perp} = \frac{-K}{\mathbf{g}}(\cos(k_o z), \sin(k_o z), 0), \quad (3.22)$$

where $K = eB/k_o mc^2$ is the dimensionless *undulator parameter*.

Equation (3.22) describes the transverse components of the electron trajectories as they pass through the undulator. It is now possible to understand how energy is transferred between the optical field and the electron beam.

2. Energy Exchange

The second Lorentz Equation, Equation (3.20), can also be written as

$$\frac{d(\mathbf{g}mc)}{dt} = -e\overrightarrow{\mathbf{b}} \cdot \overrightarrow{\mathbf{E}} \Rightarrow \frac{d\mathbf{g}}{dt} = \frac{-e}{mc} (\mathbf{b}_x, \mathbf{b}_y, \mathbf{b}_z) \cdot (E \cos(\mathbf{y}), -E \sin(\mathbf{y}), 0) \quad (3.23)$$

or

$$\frac{d\mathbf{g}}{dt} = \frac{eKE}{mc\mathbf{g}} (\cos(k_o z) \cos \mathbf{y} - \sin(k_o z) \sin \mathbf{y}), \quad (3.24)$$

$$\frac{d\mathbf{g}}{dt} = \frac{eKE}{mc\mathbf{g}} \cos(k_o z + \mathbf{y}), \quad (3.25)$$

$$\frac{d\mathbf{g}}{dt} = \frac{eKE}{mc\mathbf{g}} \cos((k + k_o)z - \mathbf{w}t + \mathbf{f}). \quad (3.26)$$

It is convenient to define the electron's position in terms of the electron phase ζ with respect to the optical field as

$$\mathbf{z} = (k + k_o)z - \mathbf{w}t, \quad (3.27)$$

so that Equation (3.26) then becomes

$$\frac{d\mathbf{g}}{dt} = \frac{eKE}{mc\mathbf{g}} \cos(\mathbf{z} + \mathbf{f}). \quad (3.28)$$

The electron phase ζ represents the microscopic electron position within the electron pulse on optical wavelength, and is an important factor describing the energy exchange between the electron beam and the optical field. When the phase $\mathbf{z} + \mathbf{f}$ of an electron falls between $\pm \pi/2$, the cosine term will be positive, resulting in energy transfer from the optical field to the electron beam. The optimum energy exchange rate is described by a resonance condition.

3. Resonance Condition

As mentioned previously, the electrons entering the undulator are moving very close to the speed of light. However, special relativity requires that the finite energy electrons travel slower than the light beam. **Resonance** is described as the condition

where, over the length of one period of the undulator, one wavelength of light passes over an electron (Figure 3.3).

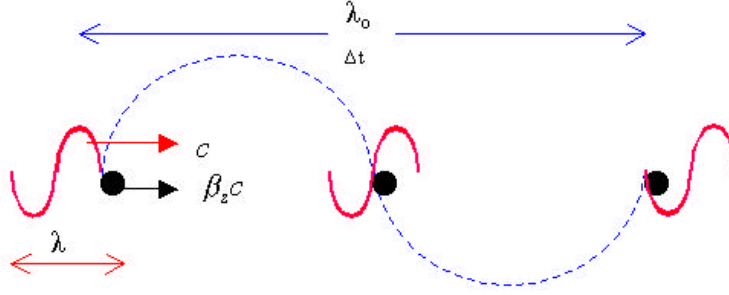


Figure 3.3. Resonance Condition. One Wavelength of Light (Traveling at Speed c), Passes over an Electron (Traveling at Speed $\beta_z c$), as the Electron Travels Through One Undulator Wavelength.

In a time interval Δt , a single electron with speed $\beta_z c$, travels distance $l_o = \beta_z \Delta t$ and a co-propagating photon distance $l_o + l = c\Delta t$, so that

$$l = \left(\frac{1 - \beta_z}{\beta_z} \right) l_o. \quad (3.29)$$

Equation (3.21) reads

$$g^2 = \frac{1}{1 - \beta_{\perp}^2 - \beta_z^2}, \quad (3.30)$$

and making use of (Equation 3.22):

$$g^{-2}(1 + K^2) = 1 - \beta_z^2. \quad (3.31)$$

Assuming $g \gg 1$ and using binomial expansion yields

$$\beta_z = 1 - \frac{1 + K^2}{2g^2}. \quad (3.32)$$

Combining Equations (3.29) and (3.32),

$$l = \frac{1 + K^2}{2g^2} l_o, \quad (3.33)$$

which demonstrates how the optical wavelength can be controlled by three parameters: the undulator wavelength, the undulator parameter (i.e., magnetic field strength) and the energy of the electron beam.

In the FEL electron beam, there are many electrons uniformly distributed in all possible electron phases \mathbf{z} as they interact with each wavelength of light. According to Equation (3.28), for a uniformly distributed electron beam, every electron, which contributes energy to the optical field, is balanced by another electron, which absorbs an equal amount of energy from the field. In order to understand this better, another important parameter, the electron phase velocity, must be discussed.

4. FEL Pendulum Equation

The rate of change of the electron phase is given by

$$\frac{d\mathbf{z}}{dt} = (k + k_o)\mathbf{b}_z c - \mathbf{w}. \quad (3.34)$$

Taking another derivative and using Equation (3.31) for \mathbf{b}_z , we get

$$\frac{d^2\mathbf{z}}{dt^2} = (k + k_o)c \left(\frac{1 + K^2}{\mathbf{g}^2} \right) \left(\frac{\dot{\mathbf{g}}}{\mathbf{g}} \right). \quad (3.35)$$

For relativistic electrons, $k \gg k_o$. Substitute $\dot{\mathbf{g}}$ from Equation (3.28) and using the resonance condition from Equation (3.33), we get

$$\frac{d^2\mathbf{z}}{dt^2} = \frac{2eKEk_o}{\mathbf{g}^2 m} \cos(\mathbf{z} + \mathbf{f}). \quad (3.36)$$

Equation (3.36) can also be written in a dimensionless form

$$\overset{\circ}{v} \equiv \frac{d^2\mathbf{z}}{dt^2} = |a| \cos(\mathbf{z} + \mathbf{f}), \quad (3.37)$$

where $\left(\overset{\circ}{\dots} \right) \equiv d(\dots)/d\mathbf{t}$, $|a| = 4\mathbf{p}NeKLE/\mathbf{g}^2 mc^2$, $a = |a|e^{i\mathbf{f}}$ is the complex dimensionless

optical field, $\mathbf{t} = ct/L$ is the dimensionless time and $\overset{\circ}{v} = \dot{\mathbf{z}} = L[(k + k_o)\mathbf{b}_z - k]$ is the dimensionless *phase velocity* (recall $L = N\mathbf{l}_o$ is the undulator length).

Equation (3.37) is called the *FEL pendulum equation* and describes an important FEL physical phenomenon called “electron bunching”. Whenever the total phase of an electron falls between $\pm p/2$, the cosine term will be positive resulting in an acceleration of the electron. When the phase is between $p/2$ and $3p/2$, the electrons decelerate. This change in phase velocity of the electrons causes the electrons to bunch. Under different conditions, just above or below resonance, the bunching occurs at different values of z . It is actually this relative location of the electron bunching that determines the net energy transfer to the optical beam. For maximum energy transfer from the beam to the optical field, “bunching” around the phase $z + f = p$ is required (according to Equation 3.28).

It can be shown that the energy change can be related to the change in phase velocity as [Ref. 11]

$$\Delta n = 4p N \left(\frac{\Delta g}{g} \right). \quad (3.38)$$

5. Phase Space Analysis

The microscopic motion of the electrons over an optical wavelength (bunching) is described by *phase-space evolution* of electrons. In order to understand how the electrons evolve in phase space, it is useful to simulate their motion over an optical wavelength based on the principal equation of motion, or the Pendulum Equation (3.37). Twenty sample electrons are initially distributed uniformly in phase from $z = -p/2$ to $3p/2$ as they enter the undulator where the interaction occurs.

In the beginning, initial electron phase velocity $n_o = 0$ is used, which corresponds to the resonance condition. In Figure (3.4), it can be seen that half of the electrons move up in the phase space plot and gain energy from the optical field, according to Equation (3.38), and half move down and lose energy to the optical field. At the end of the undulator, the electrons are bunched around $z + f = p/2$ where $f \approx 0$. The net gain is ($G \approx 0$) and the optical phase shift is small.

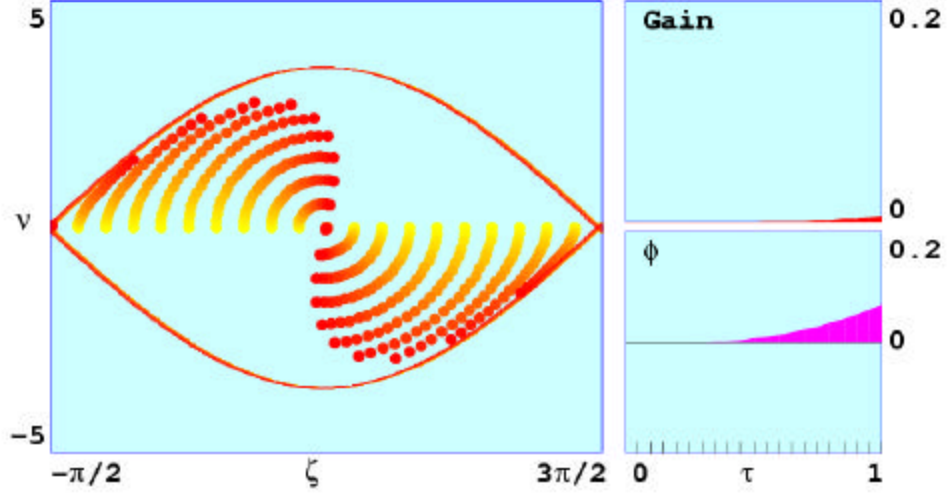


Figure 3.4. Electron Evolution in Phase Space, Optical Field Gain $G(t)$ and Phase $j(t)$ for a Single Pass through the Undulator with Electrons Injected at Resonance ($n_o = 0$).

In Figure (3.5), the evolution of twenty electrons with initial velocity $n_o = 2.6$ (above resonance) is depicted. In this case, the electrons on the left move faster than those on the right resulting in an electron bunching around $z + f = p$ ($f \approx 0$) while they also fall to lower values of n , implying a net energy transfer to the light beam. The electrons still follow pendulum phase space paths, but significant energy extraction and gain now occurs, as seen at the right.

The separatrix curve in both figures is drawn to separate the closed and opened orbits. Close orbit paths in phase space remain between $-p/2$ and $3p/2$, while open orbit path extend beyond these limits. These phase space simulations use periodic boundary conditions at $-p/2$ to $3p/2$.

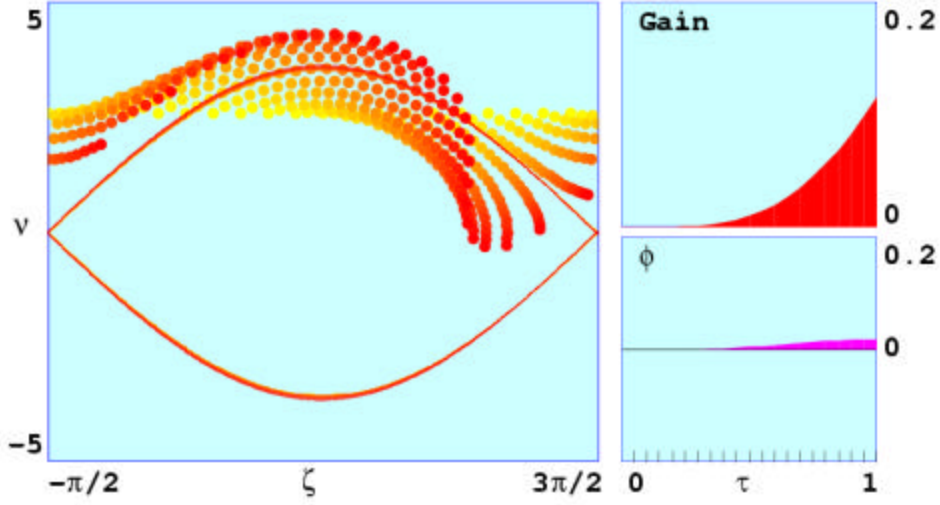


Figure 3.5. Electron Evolution in Phase Space, Optical Field Gain $G(t)$ and Phase $j(t)$ for a Single Pass through the Undulator with Electrons Injected Slightly Off Resonance $n_o = 2.6$.

After describing the electron's evolution, it is necessary to derive the wave equation that drives the optical field amplitude and phase evolution.

6. FEL Wave Equation

The optical wave equation can be derived by starting with Maxwell's wave equation in the Coulomb gauge [Ref. 18]

$$\left(\nabla^2 - \frac{1}{c^2} \frac{\partial^2}{\partial t^2} \right) \vec{A} = -\frac{4\pi}{c} \vec{J}_\perp, \quad (3.39)$$

where \vec{A} is the vector potential and \vec{J}_\perp is the transverse electron beam current. For an electron beam interacting with circular polarized light in a helical undulator, the optical vector potential is [Ref. 11]:

$$\vec{A} = \frac{E(z, t)}{k} (\sin \mathbf{y}, \cos \mathbf{y}, 0), \quad (3.40)$$

and the electron beam current is

$$\vec{J}_{\perp i} = -ec \vec{b}_\perp \mathbf{d}^3(\vec{x} - \vec{r}_i), \quad (3.41)$$

where $\mathbf{d}^3(\vec{x})$ is the three dimensional delta function and \vec{r}_i is the position of the i_{th} electron with charge e magnitude and transverse electron velocity \vec{b}_\perp given by Equation

(3.22). It can be further assumed that the optical field amplitude and phase vary slowly in time and space as that

$$\frac{\partial E}{\partial z} \ll kE, \quad \frac{\partial E}{\partial t} \ll \omega E, \quad (3.42)$$

$$\frac{\partial f}{\partial z} \ll kf, \quad \frac{\partial f}{\partial t} \ll \omega f. \quad (3.43)$$

Then, Equation (3.39) can be written

$$2\left(\frac{\partial E}{\partial z} + \frac{1}{c}\frac{\partial E}{\partial t}\right)(\cos \mathbf{y}, -\sin \mathbf{y}, 0) - 2E\left(\frac{\partial f}{\partial z} + \frac{1}{c}\frac{\partial f}{\partial t}\right)(\sin \mathbf{y}, \cos \mathbf{y}, 0) = -\frac{4\mathbf{p}}{c}\vec{J}_\perp \quad (3.44)$$

Use the two unit vectors $\hat{\mathbf{e}}_1 = (\cos \mathbf{y}, -\sin \mathbf{y}, 0)$ and $\hat{\mathbf{e}}_2 = (\sin \mathbf{y}, \cos \mathbf{y}, 0)$ to project out components of \vec{J}_\perp . Then using Equation (3.41)

$$2\left(\frac{\partial E}{\partial z} + \frac{1}{c}\frac{\partial E}{\partial t}\right) = -\frac{4peK}{\mathbf{g}} \sum_i \cos(\mathbf{y} + k_o z) \mathbf{d}^3(\vec{x} - \vec{r}_i), \quad (3.45)$$

$$2E\left(\frac{\partial f}{\partial z} + \frac{1}{c}\frac{\partial f}{\partial t}\right) = \frac{4peK}{\mathbf{g}} \sum_i \sin(\mathbf{y} + k_o z) \mathbf{d}^3(\vec{x} - \vec{r}_i). \quad (3.46)$$

The sum over all electrons can be replaced by means of an average current density \mathbf{r} times the average phase, (recall $\mathbf{y} + k_o z = \mathbf{z} + \mathbf{j}$) and Equations (3.45) and (3.46) can be rewritten as

$$\begin{aligned} \left(\frac{\partial E}{\partial z} + \frac{1}{c}\frac{\partial E}{\partial t}\right) &= -\frac{2peK\mathbf{r}}{\mathbf{g}} \langle \cos(\mathbf{z} + \mathbf{f}) \rangle, \\ E\left(\frac{\partial f}{\partial z} + \frac{1}{c}\frac{\partial f}{\partial t}\right) &= \frac{2peK\mathbf{r}}{\mathbf{g}} \langle \cos(\mathbf{z} + \mathbf{f}) \rangle, \end{aligned} \quad (3.47)$$

where $\langle \dots \rangle$ is an average over sample electrons. Equation (3.47) can be rewritten in a complex form as

$$\left(\frac{\partial}{\partial z} + \frac{1}{c}\frac{\partial}{\partial t}\right) E e^{if} = -\frac{2peK\mathbf{r}}{\mathbf{g}} \langle e^{-iz} \rangle. \quad (3.48)$$

If the optical and electron pulses are long, then the spatial dependence in the z direction can be ignored and Equation (3.48) can be simplified to

$$\overset{\circ}{a} = -j \langle e^{-iz} \rangle, \quad (3.49)$$

where \dot{a} is the derivative of the dimensionless optical field $a = |a| e^{if}$ with respect to the dimensionless time variable t , and j is the dimensionless current density $j = 8N(e\mathbf{p}KL)^2 \mathbf{r} / \mathbf{g}^3 mc^2$. Equation (3.50) is called the **FEL wave equation** and shows again that with zero average phase change and no bunching, there is no change in optical field. In order to achieve gain, electron bunching around $\mathbf{z} = \mathbf{p}$ is required.

7. Optical Gain

The FEL gain is defined as the fractional change of the optical power over one pass through the undulator. To achieve gain, energy must be removed from the electron beam and added to the optical beam. The change in energy, ΔE_e , of a single electron is given by

$$\Delta E_e = \Delta \mathbf{g} mc^2, \quad (3.50)$$

and is related to the change in phase velocity according to Equation (3.39) $\Delta \mathbf{n} = 4\mathbf{p} N \Delta \mathbf{g} / \mathbf{g}$. Assuming a monoenergetic electron beam enters the undulator with initial phase velocity \mathbf{n}_o , the average energy change, $\overline{\Delta E_e}$, can be written as

$$\overline{\Delta E_e} = \frac{\langle \mathbf{n} \rangle - \mathbf{n}_o}{4\mathbf{p} N} \mathbf{g} mc^2, \quad (3.51)$$

where $\langle \mathbf{n} \rangle$ is the average electron phase velocity at the end of the undulator.

Assuming a weak field ($|a| \ll \mathbf{p}$), low-gain ($j \leq \mathbf{p}$) FEL, the average phase velocity can be approximated using a power series expansion in $|a|$,

$$\langle \mathbf{n} \rangle = \langle \mathbf{n}^{(0)} + \mathbf{n}^{(1)} + \mathbf{n}^{(2)} + \dots \rangle. \quad (3.52)$$

Carrying out the calculations demonstrates that the average of the second order term produces the net change in the average energy [Ref. 19]

$$\langle \mathbf{n}^{(2)} \rangle = v_o + \frac{a_o^2}{v_o^3} \left[\cos(v_o t) - 1 + \frac{1}{2} v_o t \sin(v_o t) \right]. \quad (3.53)$$

Using energy conservation, the gain G can be computed as the change in energy of the electron beam in a differential volume dV divided by the initial optical beam energy in the same volume. The radiation energy in a volume element is $2E^2 dV / 8\mathbf{p}$.

To obtain the total energy change of the electron beam, Equation (3.51) must be multiplied by the number of electrons $\mathbf{r}F dV$, in that volume, where \mathbf{r} is the electron density and F is the *filling factor* (the ratio of the electron beam area to the optical beam area). The gain in the optical beam is therefore

$$G = \frac{(\mathbf{r}F dV)(\mathbf{g}mc^2 / 4\mathbf{p}N)(\langle \mathbf{n}^{(2)} \rangle - \mathbf{n}_o)}{2E^2 dV / 8\mathbf{p}}, \quad (3.54)$$

and using Equation (3.53) becomes

$$G = \frac{j}{v_o^3} [2 - 2\cos(v_o \mathbf{t}) - v_o \mathbf{t} \sin(v_o \mathbf{t})], \quad (3.55)$$

where $j = 8N(\mathbf{e}\mathbf{p}KL)^2 \mathbf{r}F / \mathbf{g}^3 mc^2$ is the dimensionless current density (now including the filling factor). Equation (3.55) shows again that the optical gain in an FEL is a function of the initial phase velocity of the electrons. As illustrated in Figure (3.4), the gain is zero at resonance ($\mathbf{n}_o = 0$). Gain reaches its maximum value when the phase velocity is $\mathbf{n}_o = 2.6$ (Figure 3.5), in full agreement with our results in the phase space analysis.

8. Efficiency

The efficiency \mathbf{h} of a Free Electron Laser is defined as the fractional loss in energy of the electron beam during one pass through the undulator [Ref. 19]

$$\mathbf{h} = -\frac{\langle \Delta \mathbf{g} \rangle mc^2}{\mathbf{g}mc^2} = -\frac{\langle \Delta \mathbf{g} \rangle}{\mathbf{g}}, \quad (3.56)$$

where $\langle \Delta \mathbf{g} \rangle$ is the average energy of an electron at the end of the undulator. Combining Equations (3.38) with (3.56) gives

$$\mathbf{h} = -\frac{\langle \Delta \mathbf{n} \rangle}{4\mathbf{p}N}. \quad (3.57)$$

This chapter describes the basic theory behind SSLs and FELs. Based on FEL theory, simulations were conducted to study the performance of the proposed high power FEL weapon design for shipboard application.

THIS PAGE INTENTIONALLY LEFT BLANK

IV. SIMULATIONS OF HIGH-POWER FREE ELECTRON LASERS

A. INTRODUCTION

A high power free electron laser for ship defense, is being designed at the Naval Postgraduate School in collaboration with Jefferson Laboratory and Advanced Energy Systems. A short Rayleigh length resonator has been proposed to increase the spot size at the mirrors, and hence reduce mirror damage. This implies a nearly concentric cavity with a very small optical mode waist. A slight misalignment of the electron beam, either an offset or a tilt, could conceivably reduce the overlap between the electrons and the optical mode in the center of the undulator, resulting in less gain and efficiency. Three-dimensional simulations are used to study the effects of off-axis shifting and tilting the electron of the electron beam. A theoretical overview on characteristic cavity modes is given before describing the design parameters and the simulations methods.

1. Optical Cavities

In order to obtain a complete description of the beams produced by a laser, the wave equation must be solved. An analytic solution to the wave equation yields electromagnetic fields that are completely specified at all points in space. A cavity mode is a field distribution that reproduces itself in relative shape and in relative phase after a round trip through the system. A complete set of modes for a laser cavity can be generated by the requirement that these modes must match the mirror surfaces [Ref. 17].

In contrast to planar mirrors, spherical mirrors provide a more stable resonator configuration for the confinement of light, less sensitive to misalignment. A spherical mirror resonator is illustrated in Figure 4.1.

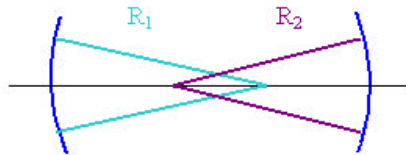


Figure 4.1. Geometry of Spherical Mirror Resonator. R_1 , R_2 are the Radiuses of Curvature of the Two Mirrors.

2. Gaussian Modes

Gaussian beams are the modes of a spherical-mirror resonator. They provide solutions to the wave equation under the boundary conditions imposed by the spherical-mirror resonator. In a vacuum, the diffraction of the optical wavefront is described by the parabolic wave equation, which, in dimensionless form, is given by [Ref. 11]

$$\frac{\partial a}{\partial t} = \frac{i}{4} \nabla_{\perp}^2 a \quad (4.1)$$

The Gaussian wave solution to (4.1) is given in non-dimensional form by [Ref. 9]

$$\begin{aligned} a(r, \mathbf{t}) &= \frac{a_o}{w(\mathbf{t})} e^{-r^2 / w^2(\mathbf{t}) z_o} e^{if(\mathbf{t})}, \\ f(r, \mathbf{t}) &= -\tan^{-1}\left(\frac{\mathbf{t} - \mathbf{t}_w}{z_o}\right) + \frac{r^2 (\mathbf{t} - \mathbf{t}_w)}{z_o^2 + (\mathbf{t} - \mathbf{t}_w)^2}, \end{aligned} \quad (4.2)$$

where $r^2 = x^2 + y^2$, $w^2(\mathbf{t}) = l + (\mathbf{t} - \mathbf{t}_w)^2 / z_o^2$ is the normalized beam width, ($w = W / W_o$) and $W^2 = W_o^2 (l + z^2 / Z_o^2)$, W_o is the beam waist radius, a_o is the dimensionless field strength at the beam waist, $\mathbf{t} = z / L$ is the dimensionless time along the undulator, \mathbf{t}_w is the position of the beam waist, $z_o = Z_o / L$ is the normalized Rayleigh length, and $Z_o = \mathbf{p} W_o^2 / l$ is defined as the distance from the beam waist over which the optical mode doubles in area.

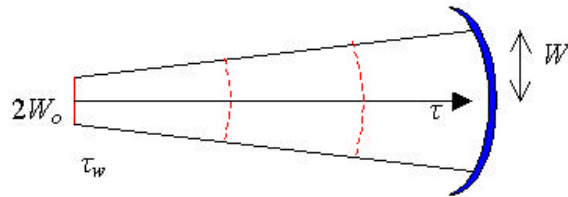


Figure 4.2. Expansion of a Gaussian Beam.

As the beam moves away from the center (\mathbf{t}_w), it spreads out by diffraction. The Rayleigh length describes how fast the beam is diffracted.

3. Resonator Optics with a Short Rayleigh Length

At the MW power levels required for a weapon design, the resonator mirrors of the oscillator are vulnerable to damage because of the small beam size. Normally the

optical mode in a FEL has a diameter of a few millimeters (~ 4 mm). Assuming 25% output coupling there is a stored power of 4 MW, so that the power density on the mirrors would be about 30 MW/cm^2 . No mirrors could survive this intensity. It is estimated that cooled sapphire mirrors with a transmitting coating can handle intensity up to 200 kW/cm^2 [Ref. 20]. A short Rayleigh length resonator has been proposed in order to increase the spot size on the mirrors and reduce the intensity. However, in that case, the optical mode waist radius becomes very small (in the nearly concentric cavity) as seen in Figure 4.3. A slight misalignment of the electron beam, either an offset or a tilt, could significantly reduce the overlap between the electrons and the optical mode in the center of the undulator, resulting in less gain and efficiency.

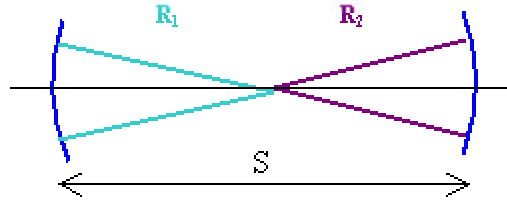


Figure 4.3. Concentric Cavity, $R_1 = R_2 = S/2$.

The goal is to design the MW FEL to fit inside the $12 \text{ m} \times 4 \text{ m} \times 2 \text{ m}$ box, which means the resonator can only be 12 m long. A Rayleigh length of $Z_o = 1.8 \text{ cm}$ increases the spot size in the resonator mirrors separated by $S = 12 \text{ m}$ to over 5 cm diameter so that the intensity on the mirrors is reduced to only about 200 kW/cm^2 .

B. HIGH-POWER FEL DESIGN PARAMETERS

The FEL design calls for a 185 Mev electron beam with a peak current of 3.2 kA, electron bunches of 0.1 mm length and a repetition rate of 750 MHz. This corresponds to a dimensionless current density of $j = 210$. The average beam current is 0.8 A, so the electron beam carries 148 MW of average power. To obtain 1 MW of output power, the FEL extraction efficiency must be at least 0.7 %.

The linearly polarized undulator consists of $N = 20$ periods, each of $I_o = 3 \text{ cm}$ length, for a total length of $L = 60 \text{ cm}$. The rms undulator parameter is $K = 2.8$, yielding an optical wavelength of $I = 1 \text{ } \mu\text{m}$. The optical cavity is $S = 12 \text{ m}$ long, with a quality factor $Q_n = 3$, ($Q_n = 1/a_n$ where a_n is the % energy lost per pass) corresponding to 28%

power transmission per pass. The Rayleigh length is $Z_o = 1.8$ cm and the optical mode waist radius is only $W_o = 0.1$ mm. The FEL design parameters listed in Table 4.1 are illustrated in Figure 4.3.

Electron beam			
Energy:	$KE = 185$ MeV	Peak current:	$I_{peak} = 3.2$ kA
Average current:	$I_{avg} = 0.8$ A	Bunch charge:	$q = 1.1$ nC
Pulse length:	$l_e = 0.1$ mm	Repetition rate:	$W = 750$ MHz
Radius:	$r_e = 0.14$ mm	Emittance:	$e_n = 24$ mm-mrad
Magnetic undulator			
Period:	$l_o = 3$ cm	# of periods:	$N = 20$
Length:	$L = 60$ cm	RMS parameter:	$K = 2.8$
Optical Resonator			
Length:	$S = 12$	Quality factor:	$Q_n = 3$
Wavelength:	$\lambda = 1$ μ m	Rayleigh length:	$Z_o = 1.8$ cm
Mode Waist:	$W_o = 0.1$ mm		
Dimensionless parameters			
Current density:	$j = 210$		
Electron beam radius:	$s_x = 0.3$	Pulse length:	$s_z = 5.0$
Rayleigh length:	$z_o = 0.03$	Mode waist:	$w_o = 0.2$

Table 4.1. High-Power FEL Parameters.

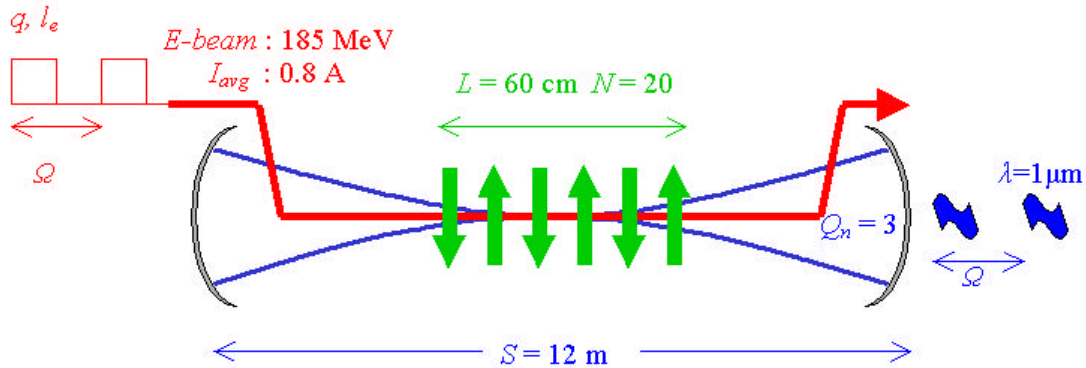


Figure 4.4. MW Level FEL Design.

C. BETATRON MOTION (LINEAR UNDULATOR)

In Chapter III, the electron motion inside the undulator was studied and the electron trajectories for a helical undulator derived assuming perfect on-axis injection of the electrons. The linearly-polarized undulator, in our design, has a field of the form [Ref. 11]

$$\vec{B}_L = B(0, \sin(k_o z) \cosh(k_o y), \cos(k_o z) \sinh(k_o y)), \quad (4.3)$$

where $k_o = 2\mathbf{p} / \mathbf{l}_o$ is the undulator wavenumber, and \mathbf{l}_o is the undulator period. The perfect electron trajectories are sinusoidal in the xz -plane, similar to the helical undulator, with no motion in the y -direction. However, when electrons drift away from the undulator axis, this undulator provides an additional long-wavelength oscillation and focusing in the y -direction called “betatron motion”.

Assuming perfect injection in the x -direction, the relativistic force in Equation (3.19) can be solved giving the electron trajectories in a linear undulator [Ref. 11],

$$\mathbf{b}_x = -\sqrt{2} \frac{K}{\mathbf{g}} \cos(k_o z) \cosh(k_o y), \quad (4.4)$$

$$\dot{\mathbf{b}}_y = -\frac{cK^2 k_o}{\mathbf{g}^2} \cos^2(k_o z) \sinh(2k_o y), \quad (4.5)$$

$$\dot{\mathbf{b}}_z = \frac{cK^2 k_o}{\mathbf{g}^2} \sin(2k_o z) \cosh^2(k_o y). \quad (4.6)$$

To remove the fast wiggling motion in the xz -plane, we average over an integral number of undulator periods \mathbf{l}_o . Averaging in the z direction yields $\overline{\mathbf{b}}_z = 0 \Rightarrow \overline{\mathbf{b}}_z \approx 1$.

The averaged equation of motion for y then becomes

$$\frac{d^2 y}{dt^2} = -\left(\frac{Kk_o L}{\mathbf{g}} \right)^2 y, \quad (4.7)$$

which describes a simple harmonic oscillator with the dimensionless betatron frequency

$$\mathbf{w}_b \equiv \frac{Kk_o L}{\mathbf{g}} = \frac{2\mathbf{p}NK}{\mathbf{g}}. \quad (4.8)$$

For a typical FEL $w_b \approx 2p$ so there is approximately one oscillation along the undulator.

The general solution to the harmonic oscillator Equation (4.7) can be written as

$$y(\mathbf{t}) = y_o \cos(\mathbf{w}_b \mathbf{t}) + \frac{L\mathbf{q}_y}{\mathbf{w}_b} \sin(\mathbf{w}_b \mathbf{t}), \quad (4.9)$$

where y_o and \mathbf{q}_y are the initial position and angle of an electron at the undulator entrance ($\mathbf{t}=0$), with respect to the undulator axis [Ref. 19]. The initial angle is related to the initial velocity by $\mathbf{q}_y = \dot{y}(0)/L$ where $\dot{y} \equiv dy/d\mathbf{t}$ and $\mathbf{t} = z/L$ is the dimensionless time along the undulator. In Equation (4.9), x_o and \mathbf{q}_x can also be included, but since the magnetic field is independent of x in Equation (4.3), any trajectory can be displaced in x without change. Equation (4.9) describes the electron betatron motion in a linearly polarized undulator with no light present. The light does not affect the betatron, but the betatron does affect the amplification of light.

The effects of both types of errors, y_o and \mathbf{q}_y can be compared using their resultant change in phase velocity. When an electron is injected off-axis by y_o or at an angle \mathbf{q}_y , its average velocity is decreased relative to an electron injected perfectly. The corresponding change in the electron's phase velocity is given by $\Delta v \approx -2pN(K^2 k_o^2 y_o^2 + \mathbf{g}^2 \mathbf{q}_y^2)/(1 + K^2)$. A beam with a random spread will begin to decrease the FEL's ability to bunch electrons, and thus decrease gain, when the average change in phase velocity becomes of order p [Ref. 11].

D. SIMULATION METHODS

To study this FEL, a three-dimensional simulation in x , y , and t is used. The undulator is oriented along the z -axis with the magnets normal to the y -axis. The simulation uses dimensionless coordinates. Longitudinal lengths in z are normalized to the undulator length L , transverse lengths in x and y are divided by $(LI/p)^{1/2}$, and angles are divided by $(I/pL)^{1/2}$.

The electrons are given an initial spread in positions (x,y) and angles $(\mathbf{q}_x, \mathbf{q}_y)$ determined by the beam emittance and focusing. They can also be given an offset in position or angle to study the effects of beam misalignment. As the electrons pass through the undulator, in addition to their fast wiggling motion in the xz -plane, they also undergo slower betatron oscillations in the yz -plane. Equation (4.9) gives the betatron motion for a single electron. For an electron beam, Equation (4.9) becomes [Ref. 4].

$$y = (y_o + \Delta y) \cos(\mathbf{w}_b(\mathbf{t} - \mathbf{t}_b)) + \frac{\mathbf{q}_{yo} + \Delta \mathbf{q}_y}{\mathbf{w}_b} \sin(\mathbf{w}_b(\mathbf{t} - \mathbf{t}_b)). \quad (4.10)$$

In this equation, the beam misalignment is described by an offset y_o , a tilt is described by an angle \mathbf{q}_{yo} , while the beam emittance is described by a random position shift of Δy and a random angular shift of $\Delta \mathbf{q}_y$. The betatron frequency is given by Equation (4.8) and \mathbf{t}_b corresponds to the position about which the beam is tilted.

In the longitudinal direction, the electrons evolve in phase space according to the FEL pendulum Equation (3.37). An electron's phase velocity is given by $v = \dot{\mathbf{z}} = L[(k + k_o)\mathbf{b}_z - k]$. If the electron is injected off-axis by a distance y and at angle \mathbf{q}_y , its phase velocity is reduced by $\Delta v = -(\mathbf{w}_b^2 y^2 + \mathbf{q}_y^2)$ [Ref. 4].

The optical wavefront is described by the parabolic wave equation,

$$-\frac{i}{4} \nabla_{\perp}^2 a + \frac{\partial a}{\partial \mathbf{t}} = -j \langle e^{-iz} \rangle. \quad (4.11)$$

The optical wavefront starts with an initial Gaussian profile, and evolves over many passes until a steady-state mode is obtained. The extraction efficiency is calculated using $\mathbf{h} = \Delta \bar{\mathbf{n}} / 4\mathbf{p}N$ from Equation (3.57), where $\Delta \bar{\mathbf{n}}$ is the average shift in electron phase velocity due to the FEL interaction.

Figure 4.5 presents a 3-D simulation of the proposed laser in x , y and \mathbf{t} . In this simulation, the electron beam enters the undulator normal to the xy -plane and no offset in position or angle is applied ($y_o = 0, \mathbf{q}_{yo} = 0$). The upper right table presents the

dimensionless parameters describing the MW level design, along with the color scale for the intensity plots of the optical amplitude $|a|$. The top-left plot, $|a(y, n)|$, presents the evolution of a slice through the optical mode over $n = 140$ passes showing how the steady-state develops. The top-center plot, $|a(x, y)|$, presents the final optical wavefront at the undulator exit $t = 1$ showing the electron beam centered in the mode. The center plot, $|a(y, t)|$, depicts a section through the optical wavefront during the final pass. The bottom left plot, $f(v, n)$, shows the development of the electron phase velocity distribution, and next to it is the final electron phase space plot at $t = 1$. The development of optical power $P(n)$ and gain $G(n)$ is in the bottom-right. The extraction efficiency was found to be $h = 2.5\%$ which is far beyond the needed value of 0.7% .

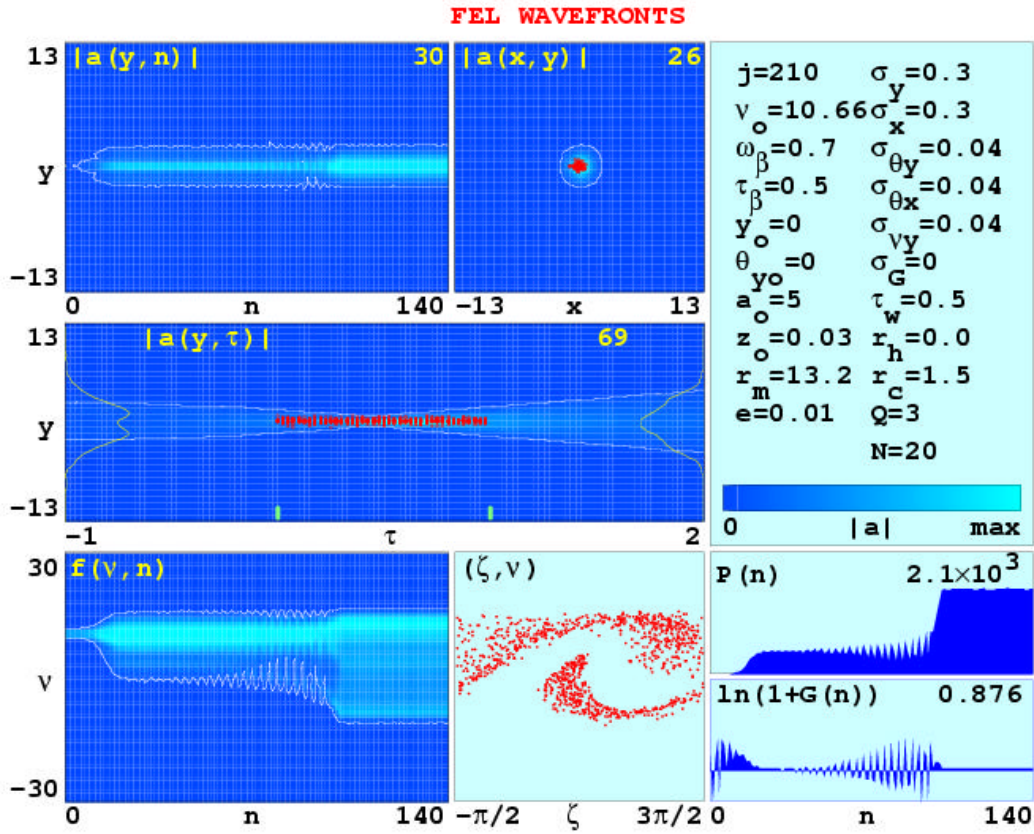


Figure 4.5. Three-Dimensional Simulation Results for the Proposed MW FEL with a Short Rayleigh Length and a Narrow Electron Beam Injected without an Offset in Position or Angle ($y_o = 0, q_{y_o} = 0$). At Saturation, the Efficiency Reaches $h = 2.5\%$.

E. SIMULATION RESULTS

Simulations were conducted to study the effects of electron beam misalignment. Specifically, the effects of tilting the electron beam are studied for two cases; tilting about the center of the undulator ($t_b = 0.5$) and tilting at the beginning of the undulator ($t_b = 0$).

1. Tilting about the Center of the Undulator ($t_b = 0.5$)

The first set of simulations was run to investigate how sensitive the FEL operation is to electron beam tilt around the undulator center as illustrated in Figure 4.6.

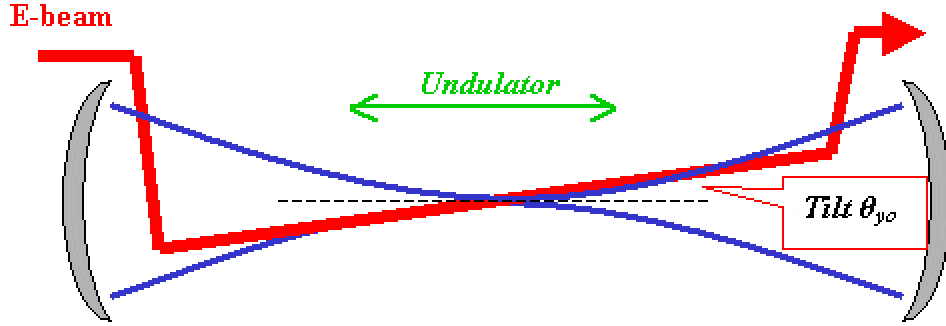


Figure 4.6. Electron Beam Tilt ($t_b = 0.5$).

Figure 4.7 shows the simulation results for steady-state efficiency η versus initial phase velocity v_o for four values of normalized electron beam tilt, $q_{yo} = 0, 2, 4, 6$, about the center of undulator. The efficiency increases up to a peak, and then drops off sharply at the value of v_o where the FEL gain falls below threshold. As the tilt angle is increased, the optimum value of v_o increases.

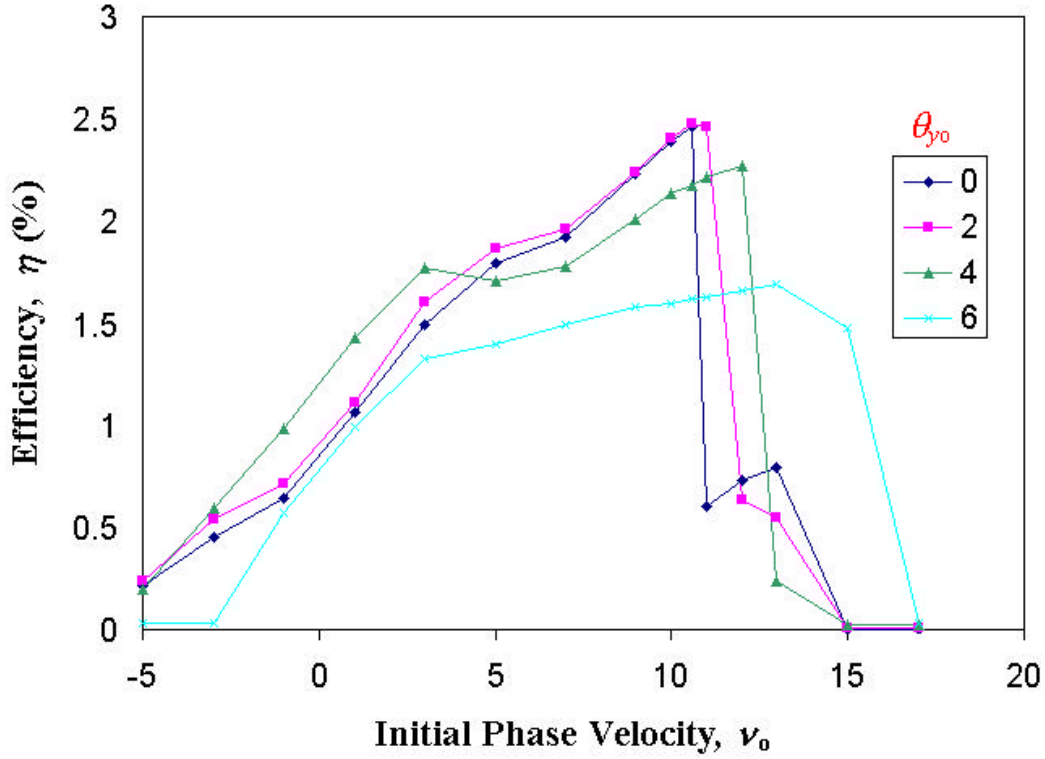


Figure 4.7. Single-Pass Extraction Efficiency, η vs Initial Phase Velocity ν_0 for Different Values of θ_{yo} through the Undulator Center ($t_b = 0.5$).

Figure 4.8 summarizes the results of many simulations, showing the peak efficiency $\hat{\eta}$ versus tilt angle q_{yo} . As the tilt angle increases, the overlap between the electrons and the optical mode waist in the center of the undulator decreases, resulting in a reduction in the FEL efficiency. The normalized tilt angle that corresponds to 1 mrad is indicated by a tickmark on the horizontal axis at $q_{yo} = 1.4$. The efficiency begins to drop off for $q_{yo} > 3$, but remains above the 0.7% goal for $q_{yo} < 8$, well beyond the design tolerance of 20 μrad , which corresponds to normalized angle $q_{yo} = 0.03$. This relative insensitivity to beam tilt is due to the fortuitous choice of tilt about the center of the undulator, where the optical fields are most intense.

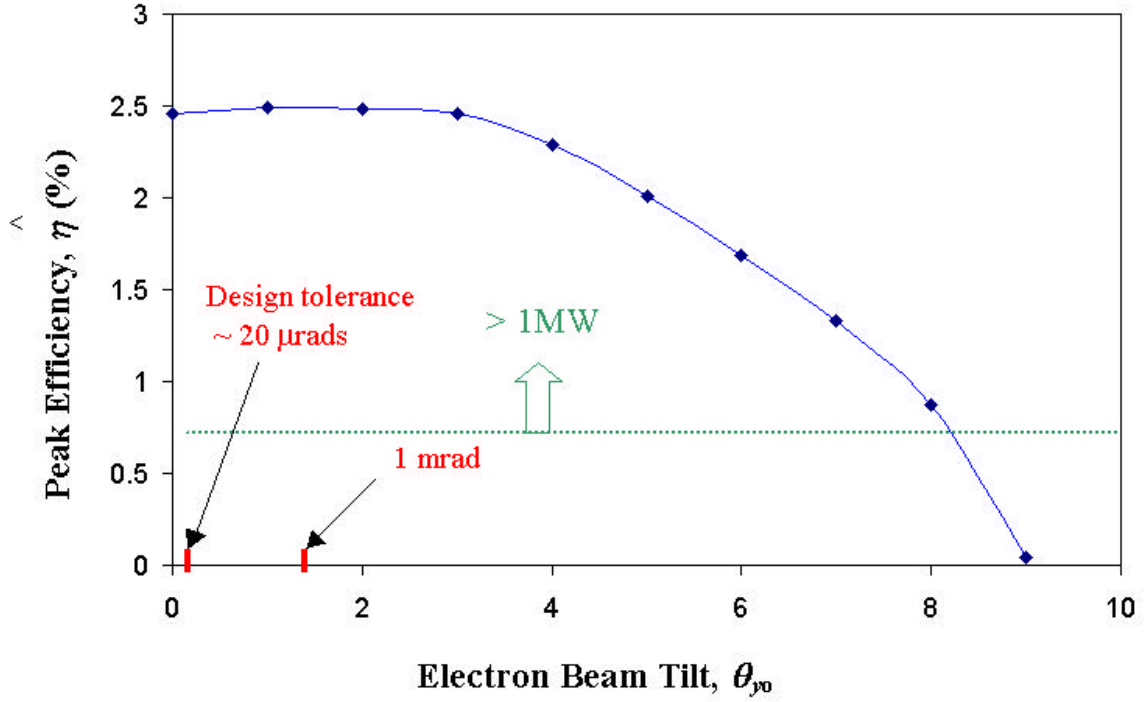


Figure 4.8. Peak Single-Pass Extraction Efficiency, \hat{h} vs. Normalized Electron Beam Tilt q_{yo} through the Center of Undulator ($t_b = 0.5$). The Required Efficiency for 1 MW Goal (0.7%) is Achieved for Tilt Angles Less than 6mrad.

A single run output corresponding to electron beam tilt $q_{yo} = 4$ and initial phase velocity $v_o = 10$ is depicted in Figure 4.9. The electron beam tilt causes the optical mode $|a(y, t)|$ to tilt about the center of undulator (center plot). The optical wave amplitude is plotted in yellow at the mirrors on each side, indicating how the power is distributed across the mirrors, and the final mode shape. The power $P(n)$ and gain $G(n)$ reach saturation after about fifteen passes (bottom-right plot). The steady-state efficiency has been decreased from 2.5% to 2.1%. The phase velocity is reduced by $\Delta v = -q_{yo}^2 \approx -16$. This implies a change in optical wavelength of about $\Delta \lambda / \lambda = \Delta v / 2pN \approx 13\%$. The electron beam energy would be adjusted to compensate if this actually occurred.

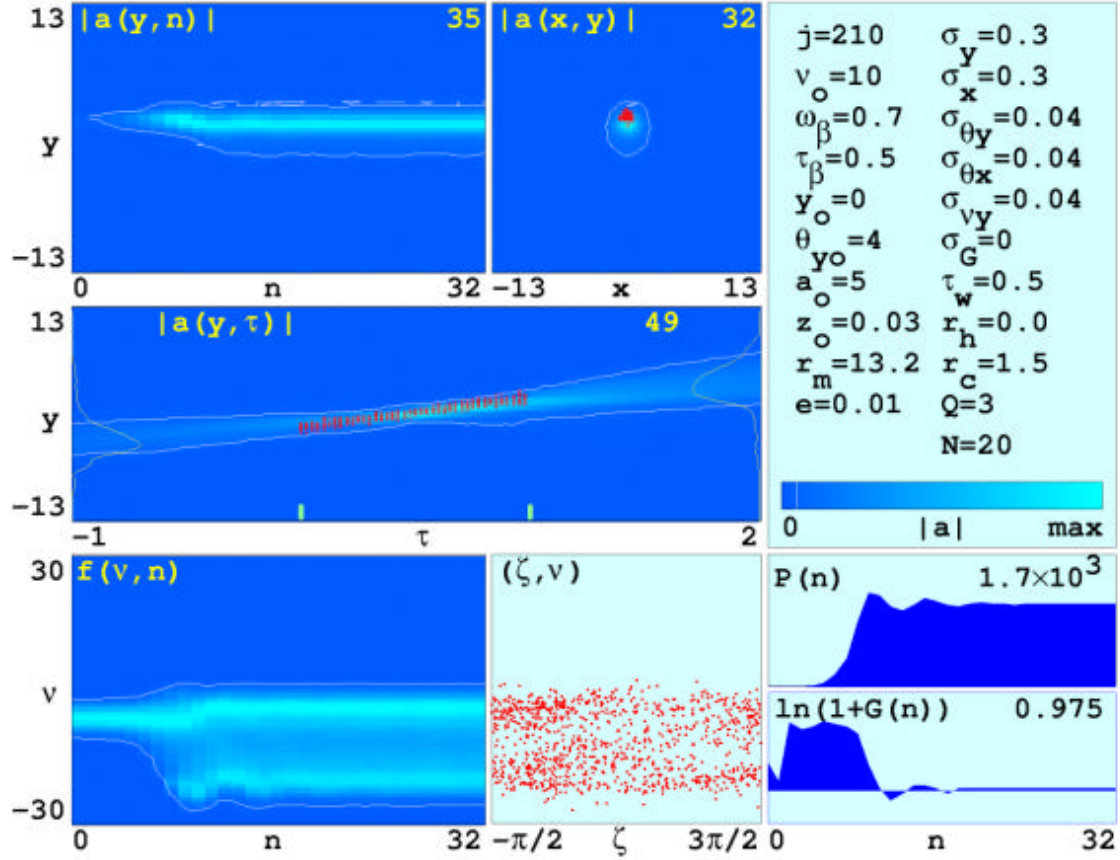


Figure 4.9. Three-Dimensional Simulation Results for an Injected Electron Beam with an Initial Tilt $q_{yo} = 4$ ($t_b = 0.5$). Efficiency Decreases to $h = 2.1\%$.

2. Tilting at the Beginning of Undulator ($t_\beta = 0$)

The second set of simulations was run to investigate how sensitive the FEL operation is to beam tilt at the beginning of an undulator as illustrated in Figure 4.10.

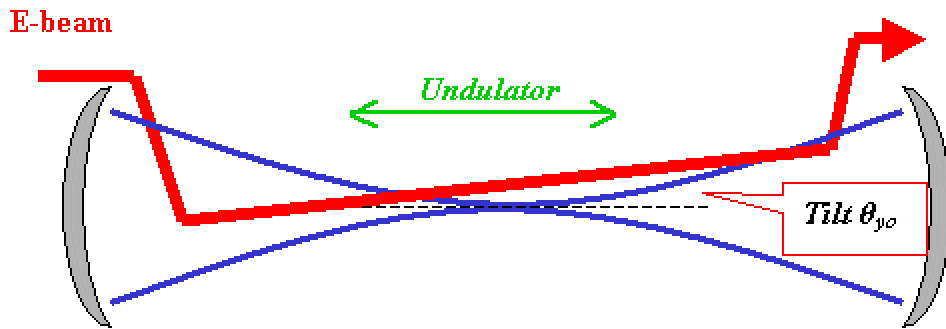


Figure 4.10. Electron Beam Tilt ($t_b = 0$).

Figure 4.11 shows the simulation results for steady-state efficiency η versus initial phase velocity v_o for three values of normalized electron beam tilt, $q_{yo} = 0, 1, 1.5$, occurring at the beginning of the undulator. The efficiency again increases up to a peak, and then drops off sharply at the value of v_o where the FEL gain falls below threshold. As the tilt angle is increased, the optimum value of v_o decreases. For $(q_{yo} = 1, v_o = 9)$ and $(q_{yo} = 1.5, v_o = 7)$, the optical mode and efficiency oscillate. A bar indicates the amplitude of oscillation.

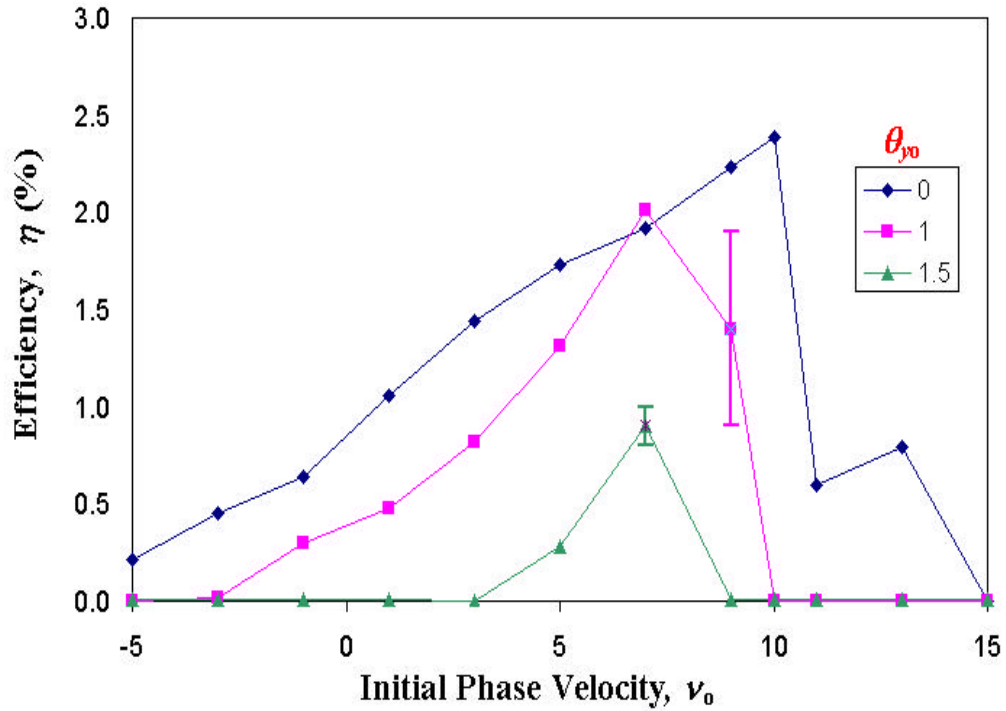


Figure 4.11. Single-Pass Extraction Efficiency, η vs Initial Phase Velocity v_o for Three Different Values of q_{yo} Occurred at the Beginning of the Undulator ($t_b = 0$).

Figure 4.12 shows the results for peak efficiency $\hat{\eta}$ versus tilt angle q_{yo} when the electron beam tilts at the beginning of the undulator. As would be expected, the FEL operation is now more sensitive to beam tilt, dropping below the MW output goal of only $q_{yo} > 1.5$, but still well beyond the experimental design tolerance.

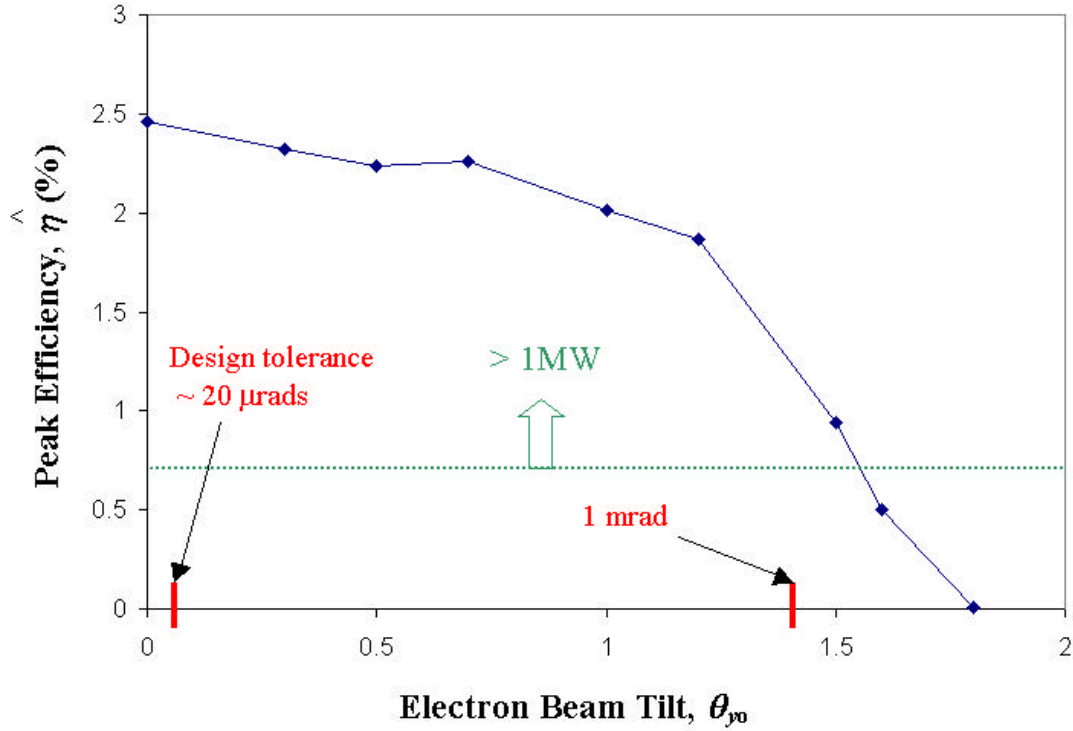


Figure 4.12. Peak Single-Pass Extraction Efficiency, \hat{h} vs. Normalized Electron Beam Tilt \mathbf{q}_{yo} at the Undulator Entrance ($t_b = 0$). The Efficiency for 1 MW Goal (0.7%) is Achieved for Tilt Angles Less than 1mrad.

A single run output corresponding to electron beam tilt $\mathbf{q}_{yo} = 1$ and initial phase velocity $v_o = 9$ is shown in Figure 4.13. The optical mode $|a(y, n)|$, and the power $P(n)$ now oscillate over many passes between two different modes. The efficiency also oscillates between 1% and 2%.

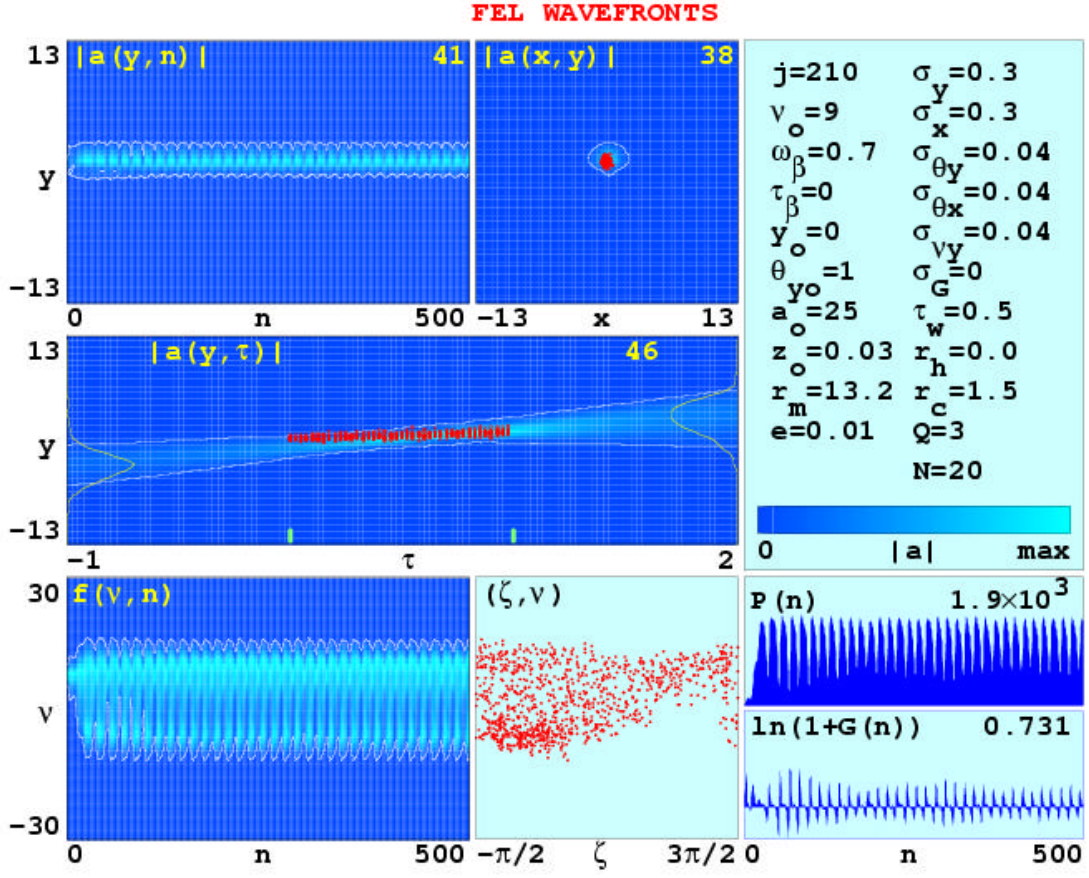


Figure 4.13. Three-Dimensional Simulation Results for an Injected Electron Beam with an Initial Tilt $q_{yo} = 1$ ($t_b = 0$). Efficiency Oscillates between 1% and 2%.

F. CONCLUSIONS

The required efficiency for the 1 MW goal, which is 0.7% for our design, is achieved in both cases for tilt angles much larger than the experimental design tolerance. The FEL operation is much more sensitive to beam tilt at the beginning of the undulator but still safely beyond the design tolerance of 20 μ rad. In both cases, the tilt angle increases the optimum value of phase velocity v_o . This change increases for $t_b = 0.5$ and decreases for ($t_b = 0$) implying a change in optical wavelength.

Simulations conducted to study the off-axis shift of the electron beam showed similar results. The MW goal is achieved for values of $y_o < 0.75$ (≈ 0.3 mm), which is well beyond the design tolerance of 0.01 mm [Ref. 4].

The proposed short Rayleigh length design, with a large spot size at the mirrors and a small optical mode waist, was found to be tolerant of electron beam misalignments and providing enough efficiency for the MW level weapon system requirements.

Additional simulations, as described in the next chapter were conducted to explore the performance of step-tapered undulator for the upcoming 100 kW upgrade in Jefferson Laboratory as a transitional step from the kW level to high power (MW level).

V. SIMULATIONS OF 100 KW FEL USING A STEP-TAPERED UNDULATOR

A. INTRODUCTION

Jefferson Laboratory has constructed and operated the world's highest average power FEL at 2.1 kW. A low risk 10 kW IR upgrade, as a next step to high power, is underway. All the hardware that is being installed for that system is believed to be capable of 100 kW operation with only slight modifications. Due to the energy recovery configuration with a recirculating electron beam, it is important to extract the maximum energy from the electron beam in a pass through the undulator while inducing the minimum amount of exhaust energy spread. A larger energy extraction reduces the requirement for a large recirculating current, while a smaller exhaust energy spread allows the intense electron beam to be recirculated without damaging components. Simulations were conducted to explore the use of a step-tapered undulator, which alters the resonance condition halfway through the undulator, in order to improve the FEL performance.

1. Short Pulses

As discussed in Chapter II, RF linear accelerators produce short electron pulses on the order of picoseconds. In general, the space-time structure of the laser beam approximately reflects the electron beam structure [Ref. 11]. Thus, an electron pulse with length l_e , will produce an optical pulse with approximately the same length. The time for an optical pulse to complete one round-trip is determined by the length of the optical cavity and is equal to $2S/c$. To keep the system running, the reflected optical pulse must be synchronized with the sequence of incoming optical pulses.

However, inside the undulator the relativistic electrons travel slightly slower than the photons. The resonance condition implies that during one pass through the undulator, the electrons will lag behind the light by the slippage distance $N\lambda$. If the electron pulse length is comparable to the slippage distance or less, then it will not overlap the optical pulse over the entire pass. As the electrons slip back relative to the optical pulse, they amplify only the trailing edge of the optical pulse. Thus, the optical pulse centroid effectively travels slower than the speed of light. Eventually, the slower moving optical

pulse centroid will “walk” entirely off the electron pulse so that no coupling can occur and the optical pulse will decay due to the cavity losses.

To compensate this effect, the optical pulse must arrive slightly ahead of the electron pulse at the beginning the undulator so it is not in exact synchronism. We define “desynchronism”, $d = -2\Delta S / N I$, the displacement between electron and optical pulses at the entrance of undulator. In practice d is adjusted by actually moving one of the resonator mirrors a small distance in order to shorten the resonator and reduce the optical pulse round-trip bounce time.

2. Tapered Undulator

In the tapered undulator, the magnetic period or magnetic field strength changes from one end to the other. It is designed to improve the extraction efficiency, at the expense of reducing the small-signal gain [Ref. 9]. In contrast to the linear tapered undulators where the magnetic field changes gradually, a *step-tapered* undulator abruptly changes the value of the field halfway through the undulator (Figure 5.1). The step-tapered undulator is described by the modified pendulum equation [Ref. 5]

$$\ddot{z} = \frac{d^2 z}{dt^2} = \Theta\left(t - \frac{1}{2}\right) \Delta + |a| \cos(z + f), \quad (5.1)$$

where

$$\Theta(z) = \begin{cases} 0 & z \leq 0 \\ 1 & z > 0 \end{cases}$$

is the step function, $\Delta = -[4pNK^2/(1+K^2)](\Delta K/K)$ is the amount of step-taper at $t = 1/2$ along the undulator, and $\Delta K/K$ is the step change in the undulator parameter.

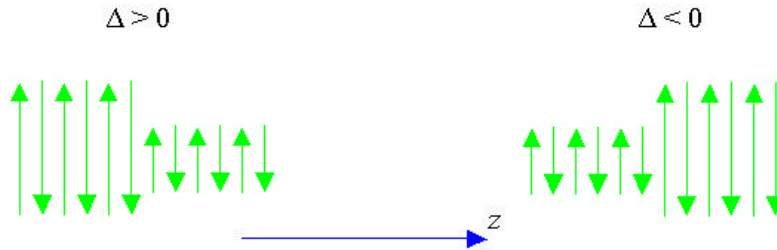


Figure 5.1. Schematic for a Step-Taper Undulator

Previously published results have shown that as much as a 75% efficiency enhancement was observed with a negative, step-tapered undulator based on simulations and experimental results from CLIO and FELIX [Ref. 5].

B. 100 KW FEL DESIGN

The 100 kW Jefferson Lab FEL design calls for a 210 MeV electron beam with a peak current of 270 A, in bunches of length 0.1 mm at a repetition rate of 750 MHz. The average electron beam power will then be 14 MW. For a 100 kW output power, an extraction efficiency of at least 0.7% is required. The 100 kW FEL parameters are listed in Table 5.1.

Electron beam			
Energy:	$KE = 210 \text{ MeV}$	Peak current:	$I_{peak} = 270 \text{ A}$
Pulse length:	$l_e = 0.1 \text{ mm}$	Repetition rate:	$W = 750 \text{ MHz}$
Magnetic undulator			
Period:	$l_o = 8 \text{ cm}$	# of periods:	$N = 36$
Length:	$L = 288 \text{ cm}$	RMS parameter:	$K = 1.68$
Optical Resonator			
Length:	$S = 36$	Quality factor:	$Q_n = 4.2$
Wavelength:	$\lambda = 1 \text{ }\mu\text{m}$		
Dimensionless parameters			
Current density:	$j = 5$	Pulse length:	$s_z = 3.0$
Step-Taper rate	$\Delta = 0, \pm p, \pm 2p$	Desynchronism:	$d = 0 \rightarrow 0.3$

Table 5.1. 100 kW FEL Parameters

C. WEAK FIELD GAIN

To study FEL gain, we use weak optical fields, where the dimensionless optical field is $|a| < p$. The desynchronism between optical and electron pulses was varied from $d = 0$ to 0.3. The gain results from many simulations with a step-tapered undulator and different values of desynchronism are plotted in Figure 5.2. The conventional non-tapered case ($\Delta = 0$) produces the highest gain of 60%. At small and large values of

desynchronism, the gain decreases for all the undulators away from peak values around $d = 0.1$. Gain for small step-taper of $\Delta = \pm p$ is only slightly reduced from the conventional case. Larger step-taper of $\Delta = \pm 2p$ causes a significant reduction in gain to around 40% peaking at lower values of $d \sim 0.05$. The FEL still works beyond the losses for larger values of $d < 0.2$.

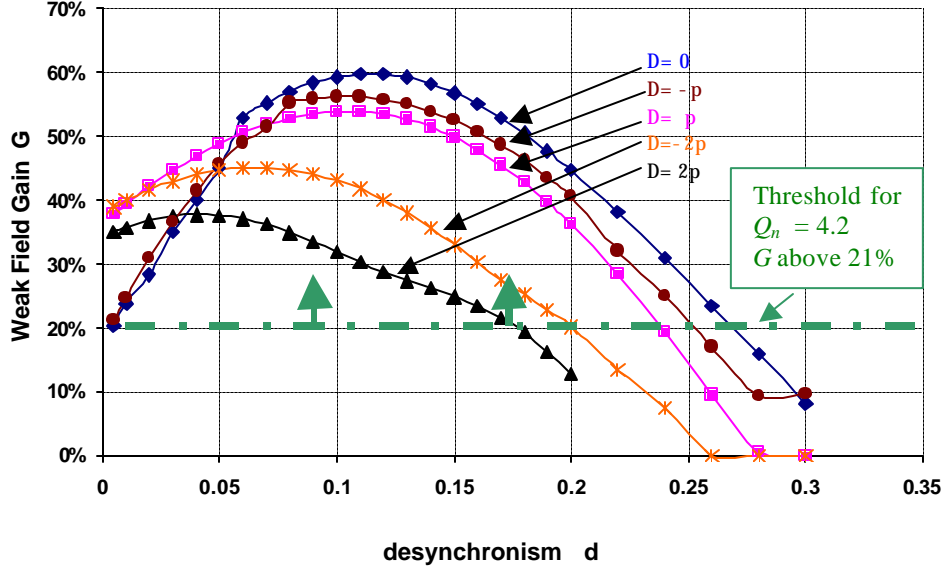


Figure 5.2. Weak Field Gain G Versus Desynchronism for Step Taper with $Q_n = 4.2$. Gain Above Threshold for All Cases, Optimum Gain with No Taper ($\Delta = 0$).

The results of this research also showed only a slight improvement in efficiency with a small negative taper ($\Delta = -p$). In all other cases explored, the efficiency is reduced compared to the conventional undulator ($\Delta = 0$) [Ref. 5].

D. ENERGY SPREAD

Figure 5.3 shows the energy spread $\Delta g/g$ plotted versus desynchronism d for different values of Δ . We found that energy spread is slightly reduced for almost all values of positive and negative taper and stays well below the limit of 15% required for recirculation in all the undulator designs.

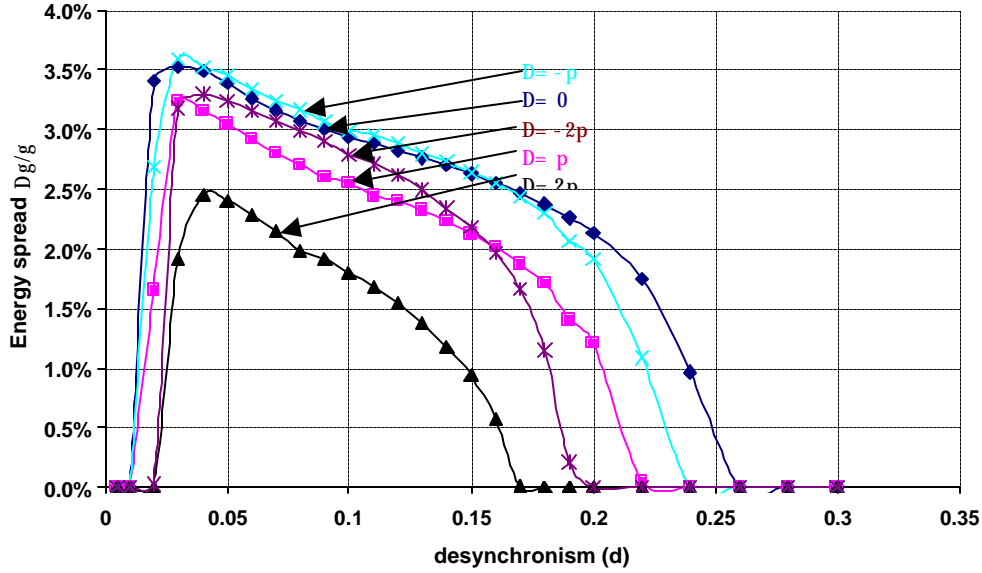


Figure 5.3. Energy Spread $\Delta g/g$ Versus Desynchronism For Step Taper with $Q_n = 4.2$. Induced Energy Spread does not Change Much with any Undulator Design.

E. CONCLUSIONS

The results of this research showed that step-taper is not always effective in increasing the FEL performance. An FEL must be far into the strong-field saturation before tapering can significantly extend the saturation limit. Only slight increase in efficiency over the conventional undulator was observed for small negative taper. The induced energy spread did not change significantly for any undulator design and was sufficiently small for recirculation. However, in all cases the gain was found to be above the threshold of 21% required for the 100 kW design.

Another important issue for operating a High Power Laser is the atmospheric propagation of the laser beam. The atmospheric effects can put more strict limits to the power requirements of the DEW systems, as described in the next chapter.

THIS PAGE INTENTIONALLY LEFT BLANK

VI. POWER SPECTRUM OF THE FEL

Earlier studies have shown that in order to destroy an oncoming missile, the laser power required on the missile surface is about 12 kW/cm² over a radius spot of $W_o = 5\text{cm}$ for a two-second duration [Ref. 18]. These numbers determine the minimum output power ($\sim 1\text{ MW}$) required in order to achieve an effective lethal FEL weapon system (ignoring the propagation losses). However, another issue of interest is how this power is to be distributed over the frequency spectrum. The extremely short (picosecond) pulse length of the FEL optical beam, a result of the short electron pulses, produces frequency components around the fundamental ($\lambda = 1\text{ }\mu\text{m}$) with significant amounts of energy. This may affect the performance of the FEL as a weapon in many ways. The concentration of energy at certain frequencies can dramatically increase the atmospheric absorption and scattering, and remove a significant amount of power from the beam. On the other hand, microwave power may result in additional damage to the target, destroying the electronics and neutralizing the guidance circuits of the missile. Finally, the effects on the visibility of the laser beam and eye-safety issues may arise.

A. FOURIER TRANSFORM OF A LASER PULSE TRAIN

Consider the output of an FEL weapon consisting of a number of optical pulses 1 psec long separated by $T = 1/W$ where $W = 750\text{ MHz}$ is the pulse repetition frequency as illustrated in Figure 6.1. The optical wavelength of the pulses is $1\text{ }\mu\text{m}$ and the total average power 1 MW. Each pulse contains several hundred wavelengths of light.

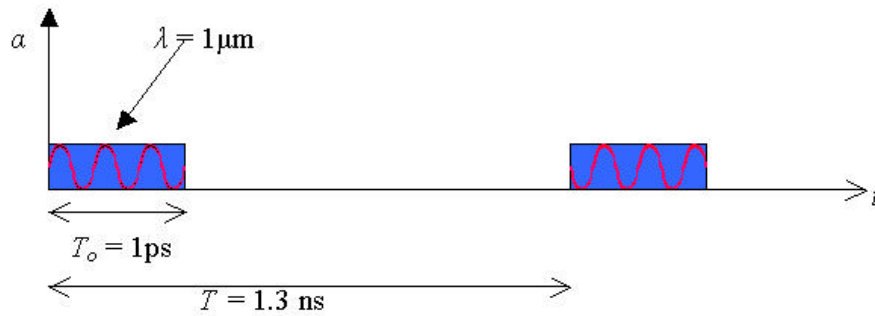


Figure 6.1. FEL Output Pulse Train.

The mathematic representation of the pulse train is

$$a(t) = \hat{a} \sum_n \Pi(t - nT) \cos(\mathbf{w}_o t + \mathbf{f}(n)), \quad (6.1)$$

where $a(t)$ is the amplitude of the electric field of the pulse with peak amplitude \hat{a} , $\Pi(t)$ is the rectangular amplitude window

$$\Pi(t) = \begin{cases} 1 & |t| \leq \frac{T_o}{2} \\ 0 & \text{otherwise} \end{cases}, \quad (6.2)$$

n is the number of pulses, $\mathbf{f}(n)$ is the random phase of the optical wave in each pulse, $\mathbf{w}_o = 2\pi f_o$ and $f_o = c/\lambda$ is the frequency of light. Since the phase $\mathbf{f}(n)$ does not contribute to the energy, and hence, to the time-average power of $a(t)$, it will be ignored for convenience sake in the calculations and a pulse train of n identical pulses considered. Thus

$$a(t) = \hat{a} \sum_n \Pi(t - nT) \cos(\mathbf{w}_o t), \quad (6.3)$$

a periodic signal with period T .

Since a 2 second burst contains 1.5 billion pulses for our problem, an infinite number of identical pulses will be considered.

In order to discover how the power is distributed in the frequency domain, the Fourier series coefficients \mathbf{a}_k of our periodic signal $a(t)$ needs to be computed. For convenience, only one pulse $\tilde{a}(t)$ is considered and the Fourier transform $A(f)$ of a single pulse computed. Then

$$A(f) = \mathcal{F}[\tilde{a}(t)] = \mathcal{F}[\hat{a} \Pi(t) \cos(\mathbf{w}_o t)].$$

Taking the Fourier transform obtains

$$A(f) = \frac{1}{2} \hat{a} T_o [\text{sinc}(f - f_o) T_o + \text{sinc}(f + f_o) T_o].$$

Based on the fundamental Fourier theory, it is known that any aperiodic signal can be viewed as a periodic signal with an infinite period. More precisely, as the period becomes infinity, the frequency components form a continuum and the Fourier series sum

becomes an integral. The relationship between the Fourier Transform of $a(t)$ and the Fourier coefficients of $\tilde{a}(t)$ is given by [Ref. 21]

$$\mathbf{a}_k = \frac{1}{T} X(f) \Big|_{f=kf_o}, \quad (6.4)$$

or

$$\mathbf{a}_k = \frac{\hat{a}T_o}{2T} [\text{sinc}(f - f_o)T_o + \text{sinc}(f + f_o)T_o] \Big|_{f=kf_o}. \quad (6.5)$$

From Parseval's relation for continuous-time periodic signals, the average power of the periodic signal is [Ref. 21]

$$P_{av} = \sum_{k=-\infty}^{+\infty} |\mathbf{a}_k|^2,$$

so that $|\mathbf{a}_k|^2$ is the average power in the k_{th} harmonic component of $a(t)$.

The above equation can also be written as

$$P_{av} = \sum_{k=-\infty}^{+\infty} \left| \frac{\hat{a}T_o}{2T} [\text{sinc}(f - f_o)T_o + \text{sinc}(f + f_o)T_o] \right|^2 \Big|_{f=kf_o}, \quad (6.6)$$

or

$$P_{av} = \sum_{k=0}^{+\infty} \left| \frac{\hat{a}^2 T_o^2}{2T^2} [\text{sinc}(f - f_o)T_o]^2 \right|_{f=kf_o}, \quad (6.7)$$

since the power exists only in positive frequencies.

Moreover, the time-average power P_{av} of $a(t)$ during the time interval T is given by

$$P_{av} = \frac{E_a}{T}, \quad (6.8)$$

where now

$$E_a = \int_{-T_o/2}^{T_o/2} \hat{a}^2 \cos^2(2\pi f_o t) dt = \frac{A^2 T_o}{2}, \quad (6.9)$$

and the sum in Equation (6.7) evaluates to

$$P_{av} = \frac{\hat{a}^2 T_o}{2T}. \quad (6.10)$$

Substituting the numbers in the above equation, the amplitude \hat{a} of each pulse can be calculated. Equation (6.7) with a simple code can now be implemented and the power spectrum of the laser beam studied.

B. POWER DISTRIBUTION

The power distribution over the frequency spectrum is depicted in Figure 6.2 (a). Most of the power is concentrated around $f_o = 3 \times 10^{14}$ MHz which corresponds to $\lambda = 1 \mu\text{m}$, while the average power substantially decreases when moving to higher or lower harmonic components. The main lobe (Figure 6.2 (b)) contains 90% of the total power of the laser beam, $P_{ml} \approx 0.9$ MW.

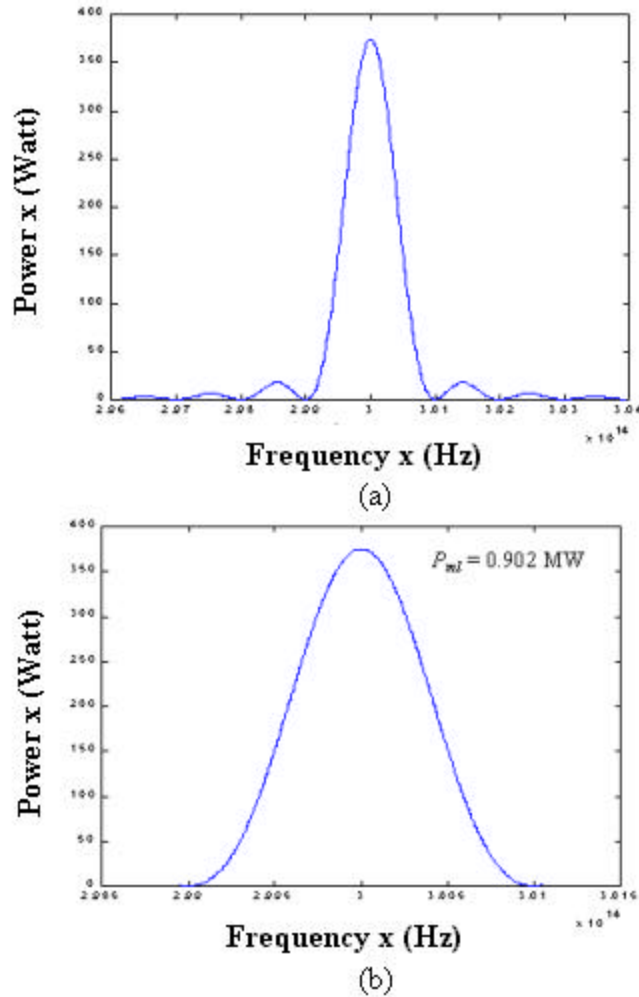


Figure 6.2. Power Spectrum around 1 μm (a), Main Lobe (b).

Thus, a huge amount of power ($\approx 10^5$ W) is contained in other frequency components as illustrated in Figure 6.3.

The frequency region between $f = 10^{12}$ Hz and $f = 10^{17}$ Hz contains almost 99.99% of the total power of the beam while the power in the harmonics outside this region is negligible.

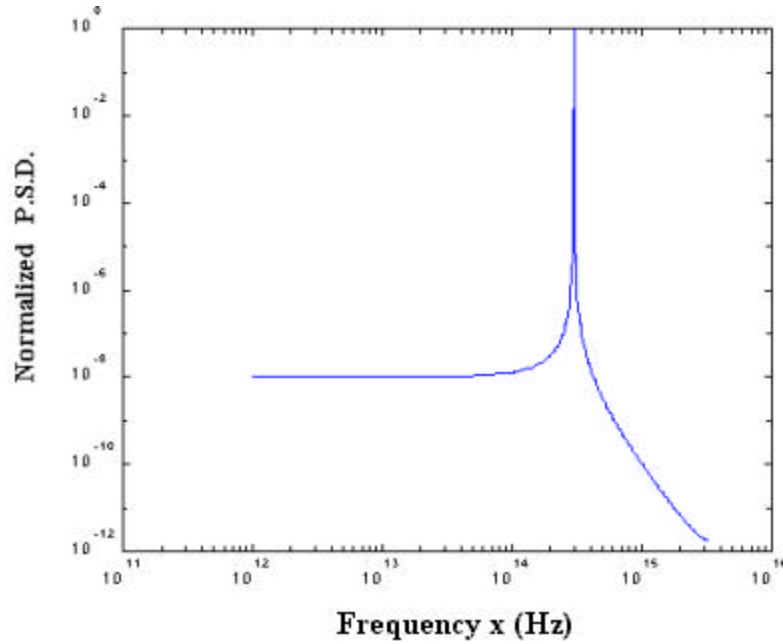


Figure 6.3. Normalized Power Spectral Density of the FEL Beam.

Specific frequency ranges of interest can now be further studied.

1. Microwave Regime

The microwave region is very important as a significant amount of power in microwaves could cause a catastrophic failure to control and navigation electronics of the target missile. However, the power contained in the microwave region ($\lambda = 1$ mm to $\lambda = 1$ m) is found to be too little to result in a kill mechanism, $P_{mic} = 0.085$ Watts (Figure 6.4). Thus, the FEL weapon is not expected to seriously affect and disorient an incoming cruise missile through the microwave region of its spectrum.

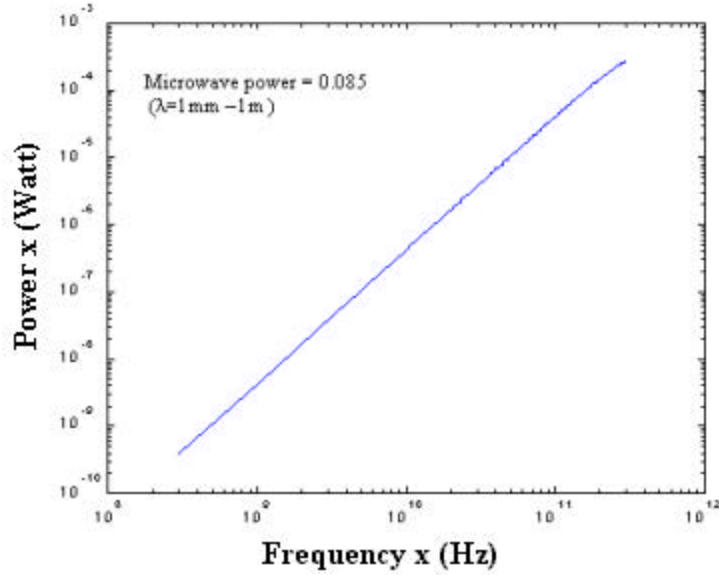


Figure 6.4. Power Spectra in Microwave Regime.

2. Visible Spectrum

Contrary to the microwave regime, the visible region is located very close to the near infrared, where the fundamental ($1 \mu\text{m}$) is located, and thus, a significant amount of power is contained in this region. Figure 6.5 depicts the power spectral density in the visible region ($I = 400\text{nm}$ to $I = 780\text{nm}$). The total power contained in the visible region is found to be $P_{vis} \approx 500 \text{ W}$ for the square optical pulse.

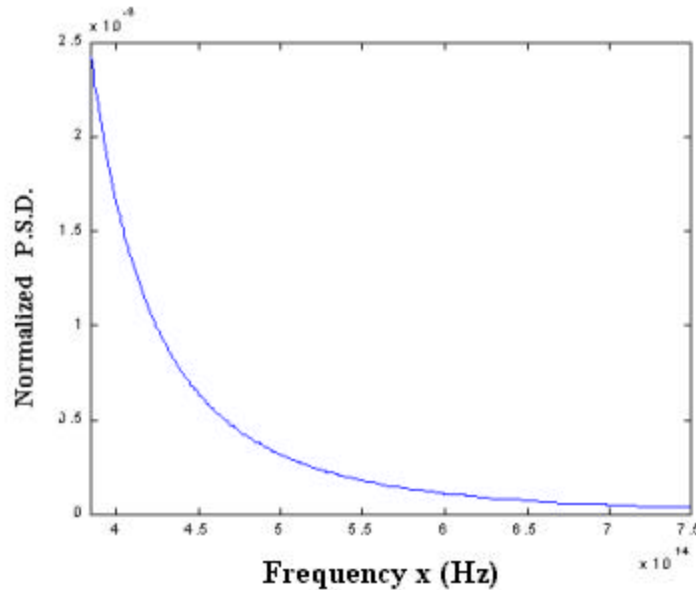


Figure 6.5. Power Spectral Density in the Visible Region.

Now, it can further estimated if the FEL beam will be visible to the naked eye. In the configuration of Figure 6.6, a 1 MW FEL burst against an oncoming missile 5 km away from the beam director is considered.

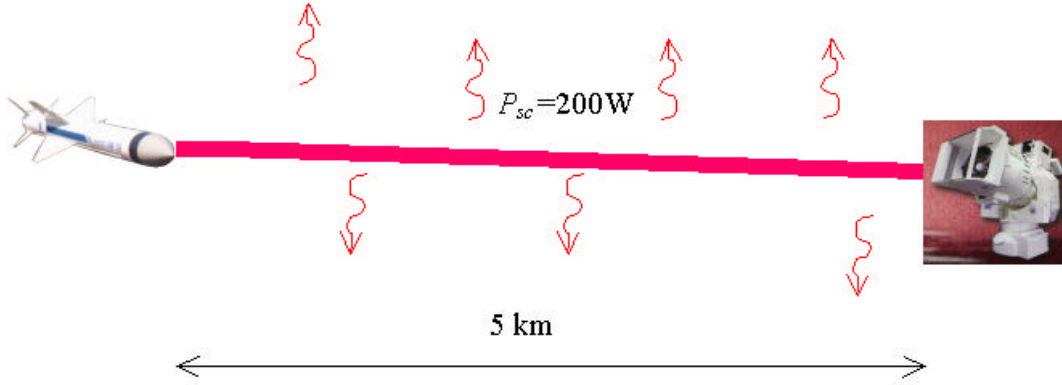


Figure 6.6. Scattered Power in the Visible Spectra.

First, it is necessary to compute the total visible power scattered through the atmosphere along the beam path. In the optimum case of no clouds or fog, the scattering rate in the visible region is $a_{sc} = 0.1/ \text{ km}$ (Figure 6.7). The scattered power is given by [Ref. 22]

$$P_{sc} = P_{vis}(1 - e^{-a_{sc}z}), \quad (6.11)$$

where P_{sc} is the scattered power in the visible region and $P_{vis} = 500W$. For $z = 5 \text{ km}$, $P_{sc} = 200W$ is obtained.

Assuming that the light scatters uniformly in all directions, the intensity of the scattered light is given by

$$I_{sc} = \frac{P_{sc}}{S_b} = \frac{P_{sc}}{2\pi rz}, \quad (6.12)$$

where r is the average radius of the beam ($r = 10 \text{ cm}$) and S_b the total external surface area of the beam. From Equation 6.12, $I_{sc} = 0.06 \text{ W/m}^2$ or 60 nW/mm^2 . For the human eye, the radius of the pupil is 2 mm and the pupil area 3 mm^2 [Ref. 23]. Assuming that

the observer is stationed right next to the beam path, the fraction of light entering the eye is then $P_{eye} = I_{sc} \times 3 \text{ mm}^2 = 180 \text{ nW}$.

If the divergence of scattered light as well as the propagation losses between the FEL beam and an observer are now considered, it is thus observed that the power level entering the eye is even lower and unlikely to be detected at any reasonable distance (even several meters).

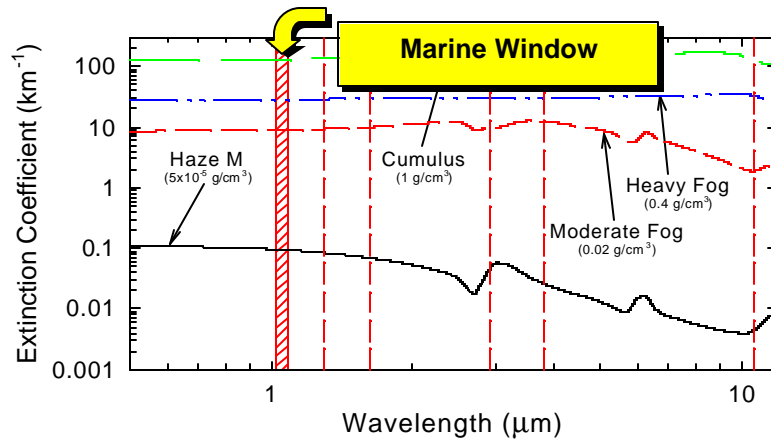


Figure 6.7. Aerosol Scattering. (From [Ref. 1])

C. ATMOSPHERIC EFFECTS

Many of the challenges in developing a HEL weapon system that will operate in a maritime environment are related to atmospheric effects and propagation. Of primary concern to the Navy are the effects of high aerosol scattering on the propagation of the HEL beam from the source to the target. Natural aerosols including fog, precipitation, and clouds must be considered in any planned use of laser weapons. On the battlefield, airborne dust thrown up by exploding ordnance and smoke from burning equipment, may also occur.

On the other hand, absorption by atmospheric gases and aerosols can generate atmospheric density gradients that cause the laser beam to spread out. This effect is known as thermal blooming.

It is generally understood that scattering effects become more significant as the laser wavelength shortens (Figure 6.7). However, scattering is a linear process and depends on the index of refraction and the mean particle size. In contrast, absorption

leads to non-linear losses for high-energy lasers, where an increase in power from the laser results in an increasing percentage of energy loss. Thus, an atmospheric window with low absorption is important for minimizing thermal blooming.

At the moment, $\lambda = 1 \mu\text{m}$ seems to be the best compromise wavelength between scattering and blooming and has been chosen as the operating FEL wavelength. Absorption and scattering are the primary causes for loss of energy in the atmosphere, but they must be studied in detail to understand their effects on weapon system performance.

1. Power Removal (Pulse Distortion)

The energy losses due to aerosols are described by $e^{-a_e z}$ where a_e is called the “extinction coefficient” and represents the aerosol attenuation due to both absorption and scattering as a function of wavelength. In reality, the maritime conditions at a particular geographic location may vary on different days. The extinction coefficient has been described by computer modeling codes such as FASCODE, LOWTRAN, MODTRAN, and MOLLY.

All of these codes allow the user to insert weather conditions and select from different environments. It is obvious that different conditions can lead to different results. For the purpose of this work, a specific maritime aerosol model for a moderately clear atmosphere will be considered (Figure 6.8).

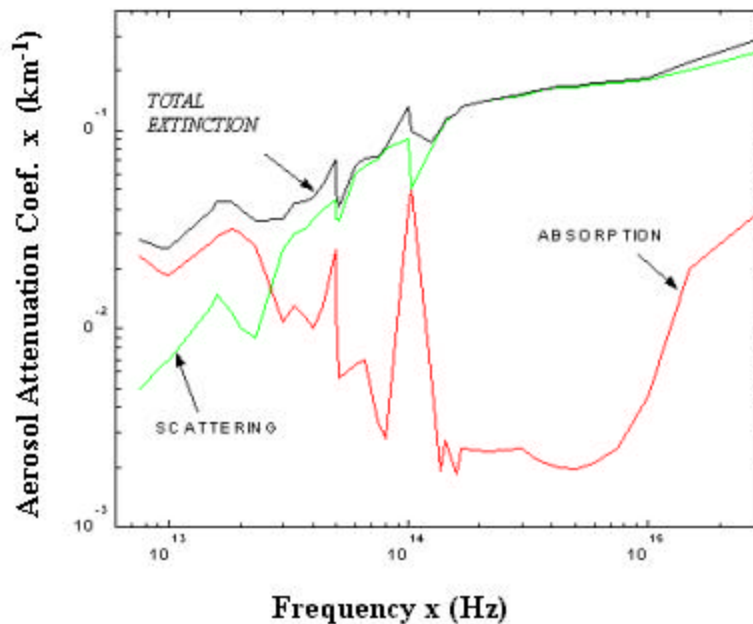


Figure 6.8. Maritime Aerosol Model (23 km Visibility). (After [Ref. 24])

It was demonstrated previously that the short pulses of the FEL beam lead to a broadband spectrum with significant power in harmonics far from the fundamental ($\lambda = 1 \mu\text{m}$), where each one has a different value of extinction.

Since the power contained in each wavelength is known, the aerosol attenuation coefficients can be applied to the FEL beam power spectra and the total power P_{mis} that can be delivered from a laser to the target computed

$$P_{mis} = \sum_I P_{ship}(I) e^{-a_e(I)z}, \quad (6.13)$$

where $P_{ship}(I)$ is the laser beam output power corresponding to each wavelength.

The amount of power that is delivered through the atmosphere over a distance $z = 5 \text{ km}$ using the specific model is found to be $P_{mis} = 0.47 \text{ MW}$. Thus, even though 1 MW is enough to destroy an incoming missile, atmospheric effects result in significant reduction in on-target irradiance so that lethal effects may not be obtained (Figure 6.9).

The total power on the target could be actually increased if the FEL operated at shorter wavelengths. As can be seen in Figure 6.7, by shifting to longer wavelengths (lower frequencies), the main lobe, which contains the 90% of the total power, can be moved to smaller values of extinction, since this is basically determined by the scattering coefficient. However, when moving to regions with high atmospheric absorption the problem of thermal blooming arises.

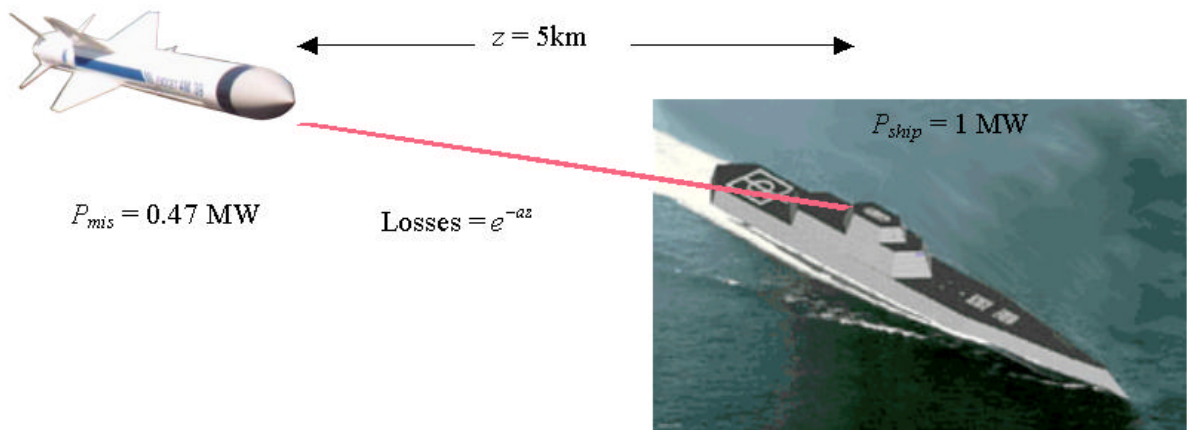


Figure 6.9. Power Removal.

2. Thermal Blooming

During an engagement, the path of the laser beam column may include a region of stagnate air. The existence and the length of a stagnation zone cannot be predicted precisely, but statistically it is expected to be between 1 m – 100 m long [Ref. 24]. The thermal blooming effect is created by molecular absorption when the laser beam propagates through such a stagnation zone in the atmosphere. The absorbed power in this zone leads to temperature rise and, thus, to a change in the index of refraction. Accordingly, a difference in the index of refraction changes the speed of light and, thus, the optical path length across the beam wavefront. In other words, light travels slower due to low temperatures, higher air density on the outer portion of the laser beam and faster due to higher temperatures, lower air density, inside the laser beam. This effect, which is analogous to a negative lens, spreads the laser beam and can cause catastrophic phenomena during high-energy laser beam propagation.

Thermal blooming is a non-linear effect. Since the temperature rise is proportional to the absorbed power, it can be seen that more power leads to more blooming. Minimizing the absorption is important to the performance of the laser as a weapon.

The amount of power absorbed from the atmosphere can be computed by knowing the power spectrum of the laser beam. The limiting consequences of thermal blooming may then be evaluated for an FEL weapon system [Ref. 25].

In closing this section, it must be mentioned that absorption and scattering are generally incorporated in analysis using statistical averages. In reality, maritime conditions, at a particular geographic location and at a particular time, may favor different wavelengths on different days. The solution to this problem can be the use of an FEL, which even at high power levels, could be pre-designed to operate at different wavelengths. This option which is not possible with solid-state or chemical lasers.

D. GAUSSIAN SHAPE PULSES

It has been demonstrated how the power of an FEL beam is distributed throughout the frequency spectrum as well as how the power spectrum can provide important information about the atmospheric propagation effects. However, in our calculations, a

laser beam consisting of *rectangular micropulses* has been considered, since the amplitude \hat{a} is a positive constant. In reality, Gaussian-shaped, or smooth electron pulses from the accelerator will produce Gaussian-shaped, or smooth, or similarly optical pulses.

At this point, it is instructive to consider the effect of the shape of the micropulse on the power spectrum of the laser beam. The discontinuities that appear in the rectangular pulse shape result in high sidelobes in the frequency domain. In contrast, pulses that do not contain abrupt discontinuities have correspondingly low sidelobes in their frequency spectra.

In order to observe the differences, the power spectral density of two micropulses with different shapes will be computed. To represent a Gaussian shape pulse, which actually extends from $-\infty$ to $+\infty$, a very common pulse shape in digital filtering design, the *Hanning pulse*, can be used instead as can be seen in Figure 6.10 [Ref. 26].

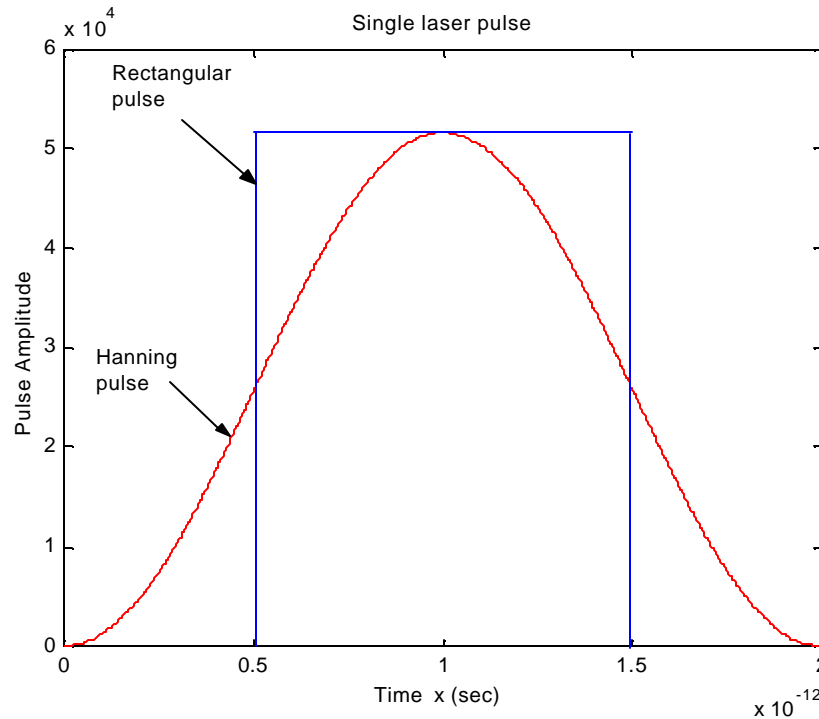


Figure 6.10. A CW Pulse with (a) Rectangular Envelope (in Blue), (b) Using a Hanning Pulse (in Red).

The “bell-shape” pulse is twice as long as the rectangular one and contains no discontinuities while falling off smoothly. The power spectral densities of both micropulses are illustrated in Figure 6.11.

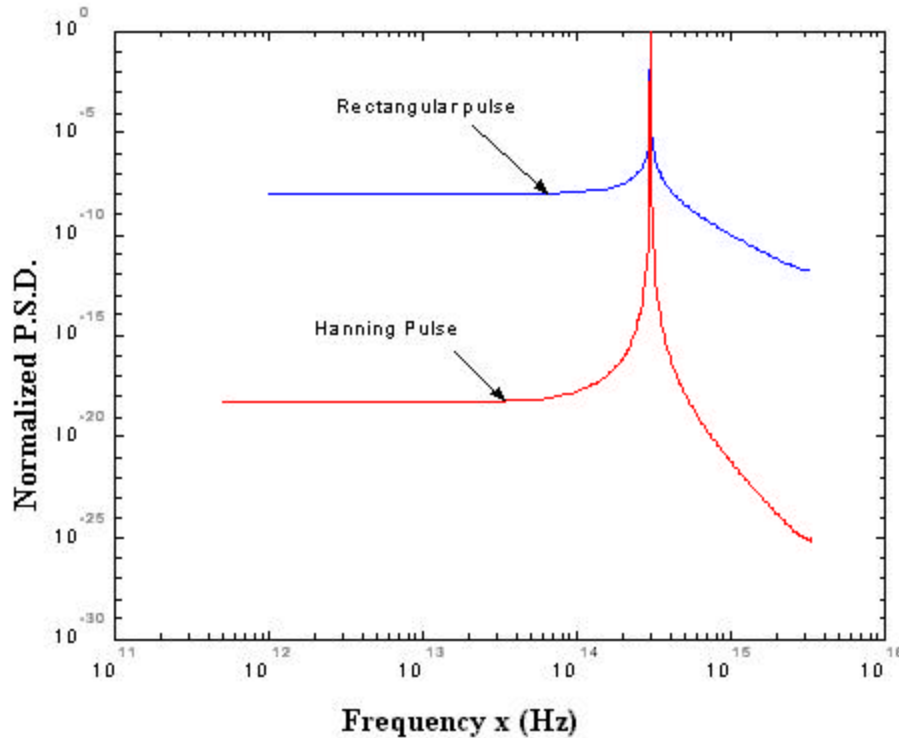


Figure 6.11. Normalized Power Spectra Density of a micropulse (a) Rectangular Envelope (in Blue), (b) Hanning Pulse (in Red).

It can be seen that using the Hanning pulse shape significantly lowers sidelobes compared to the rectangular window, while more power is concentrated into the main lobe or around the fundamental frequency. This means that, in reality, there will be less power in the harmonics far from the fundamental than computed earlier considering the rectangular pulses. The concentration of the beam energy around the selected frequency is obviously desirable and expected to ameliorate the negative effects of atmospheric absorption and aerosol scattering. Rectangular envelope pulses correspond to the worst case as far as the broadening of the spectrum is concerned, and can just provide indicating values of the power spectrum of the FEL beam.

E. CONCLUSIONS

This chapter shows how the power of the FEL is distributed over the frequency spectrum. The atmospheric absorption and scattering for the specific maritime aerosol

model showed a power removal of 53% over a distance of 5 km. However different laser pulse shapes can give different results since as the pulses gets smoother more power is concentrated on the main lobe around the fundamental frequency. The next Chapter outlines the conclusions of the whole research.

VII. CONCLUSIONS

High-energy lasers provide the Navy with unique opportunities to augment or improve operational capabilities in a variety of mission areas. The most likely candidates for the development of a Navy high-energy weapon system are the high power Free-Electron Lasers (FELs) and Solid-State Lasers (SSLs) for three reasons:

- These are both all-electric lasers, and there are inherent dangers associated with the storage of the chemicals needed for chemical lasers on board ship;
- The need to develop a source at the appropriate wavelength for maritime propagation, and present-day chemical lasers are at the wrong wavelength;
- The Navy's recent decision early in 2000 to adopt an electric drive propulsion system for DD-21 and follow-on ships is consistent with these two all-electric lasers.

In general, FELs can produce powerful, highly coherent, optical beams, but also place extreme demands on the resonator mirrors. SSLs, typically, produce a larger beam spot on the mirrors, requiring optics with a lower damage threshold, but they generally do not achieve the desirable beam quality. Efficient heat removal from the laser media is needed in high-power SSL designs, while high-power FELs require a high-brightness injector and novel optical cavity designs. However, with adequate research development efforts, it appears that both technologies have the potential to meet the needs of a weapon-class laser.

Fiber optic lasers and the Heat Capacity Laser project are examples of the readiness of solid state laser technology for rapid maturation. On the other hand, the unique advantages of FELs, such as wavelength selectability and tunability, high beam quality, the potential to achieve high peak power without distorting the lasing media and long run-time, could favor FELs for weapon-class lasers in the near future.

At the Naval Postgraduate School, a high power free electron laser for ship self-defense is being designed with a short Rayleigh length, which results in large spot sizes at the mirrors to avoid mirror damage. Three-dimensional simulations used to study the performance of the proposed design demonstrated that it is tolerant of electron beam

misalignments, and provides high enough extraction efficiency for the MW level weapon system requirements.

The required 0.7% efficiency for the 1 MW goal is achieved in simulations for tilt angles much larger than the experimental design tolerance. It is found that FEL operation is much more sensitive to beam tilt at the beginning of the undulator than tilting around the middle, but it is still safely beyond the design tolerance.

Simulations were also conducted for the 100 kW FEL design as a transitional step to high power. The results of this research showed that weak field gain exceeds the required threshold of 21%, while the strong-field energy spread did not change significantly over any undulator design.

Finally, the spectrum of the proposed FEL output was studied. The power is distributed over a wide frequency range. It was found that 90% of the total power is concentrated in the main lobe (around 1 μm wavelength), while power decays sharply for higher or lower harmonics. Atmospheric absorption and scattering were also studied for a specific maritime aerosol model showing power removal of 53% up to a distance of 5 km. However, the effects of Gaussian-shaped pulses showed that there will be less power in the harmonics far from the fundamental than computed considering the rectangular pulses. The concentration of the beam energy around the selected frequency is obviously desirable and expected to ameliorate the negative effects of atmospheric absorption and aerosol scattering.

LIST OF REFERENCES

- [1] Roger D. McGinnis, "High Energy Lasers Efforts," PMS 405 Presentation, NPS, March 19, 2002.
- [2] A. M. M. Todd, Advanced Energy Systems, "MW FEL System Modeling", NPS Presentation, May 23, 2001.
- [3] Defense Science Board Task Force on High Energy Laser Weapon Systems Applications, Final Report, Washington D.C., June 2001.
- [4] J. Blau, V. Bouras, A. Kalfoutzos, G. Allgaier, T. Fontana, P. P. Crooker, and W. B. Colson, " Simulations of High Power Free Electron Lasers with Strongly focused Electron and Optical Beams," accepted by *Nucl. Instr. and Meth* (2002).
- [5] J. Blau, V. Bouras, W. B. Colson, K. Polykandriotis, A. Kalfoutzos, S. V. Benson, and G. R. Neil, "Simulations of the 100 kW TJNAF FEL Using a Step-tapered Undulator," *Nucl. Instr. and Meth.* A483, pp. 138-141, (2002).
- [6] High Energy Laser Executive Review Panel, DOD Laser Master Plan Vol. II, August 2000.
- [7] Eli Zimet – ONR Chairman, "High Average Power Free Electron Laser Technology Assessment Report," FEL Working Group, May 2000.
- [8] Free Electron Laser Development for Naval Applications Workshop, Workshop Report, Virginia, June 2001.
- [9] H. P. Freund and G. R. Neil "Free Electron Lasers: Vacuum Electronic Generators of Coherent Radiation," *Proceedings of the IEEE*, Vol. 87, No. 5, pp. 782-803 May 1999.
- [10] A. M. M. Todd, H. Bluem, and G. R. Neil "Superconducting RF Injector for High- Power Free-Electron Lasers," *Particle Accelerator Conference 2001. Proceedings of the 2001*, Vol. 1, pp. 92-94 (2001).
- [11] W. B. Colson, C. Pellegrini, and A. Renieri, *Laser Handbook*, Vol. 6, Elsevier Science Publishers B. V North-Holland, Amsterdam, (Chapter 5), 1990.

- [12] W. B. Colson, NPS “Free Electron Laser Analysis, Modeling and Simulation,” Presentation, June 2002.
- [13] S. O. Kasap, *Electronic Material and Devices*, Second Edition, McGraw-Hill, New York, 2002.
- [14] W. Koechner, *Solid-state Laser Engineering*, Fifth Edition, Springer, New York, 1999.
- [15] Y. Hirano, T. Yanagisawa, S. Ueno, and T. Tajime “All-solid-state high-power conduction-cooled Nd:YFL rod laser,” *Optics Letters*, Vol. 25, No. 16, p. 1168, August 2000.
- [16] E. A. Saleh, and M. C. Teich, *Fundamental of Photonics*, Wiley-Interscience, New York, 1991.
- [17] J. T. Verdeyen, *Laser Electronics*, Third Edition, Prentice Hall, New Jersey, 2000.
- [18] R. D. McGinnis, “Free Electron Lasers for Directed Energy,” PhD Dissertation, Naval Postgraduate School, Monterey, California, December 2000.
- [19] J. Blau, “Multimode Simulations of Free Electron Lasers,” PhD Dissertation, Naval Postgraduate School, Monterey, California, March 2002.
- [20] W. B. Colson, A. M. Todd, and G. R. Neil, “FEL with Short Rayleigh Length,” *Nucl. Instr. and Meth.* A483, p. II-9 (2002).
- [21] Alan V. Oppenheim, Alan S. Willsky, and S. Hamid Nawab, *Signals and Systems*, Second Edition, Prentice Hall, New Jersey, 1996.
- [22] E. L. Dereniac, and G. D. Boreman, *Infrared Detectors and Systems*, Wiley-Interscience, New York, 1996.
- [23] E. Hecht, *Optics*, Third Edition, Addison Welsey Longman, New York, 1998.
- [24] W. B. Colson, Notes for PH 4911 (Simulations of Physical and Weapon Systems), NPS, 2002 (unpublished).

- [25] A. Kalfoutzos, “Free Electron and Solid State Lasers Development for Naval Directed Energy” Master’s Thesis, Naval Postgraduate School, Monterey, California, December 2002.
- [26] J. G. Proakis, and D.G. Manolakis, *Digital Signal Processing*, Third Edition, Prentice Hall, New Jersey, 1996.

THIS PAGE INTENTIONALLY LEFT BLANK

INITIAL DISTRIBUTION LIST

1. Defense Technical Information Center
Ft. Belvoir, Virginia
2. Dudley Knox Library
Naval Postgraduate School
Monterey, California
3. Professor William B. Colson, Code PHCW
Department of Physics
Monterey, California
4. Professor Phillip E. Pace, Code EC/PC
Department of Electrical and Computer Engineering
Monterey, California
5. Professor Joseph Blau, Code PHBL
Department of Physics
Monterey, California
6. Professor Peter Crooker, Code PHCP
Department of Physics
Monterey, California
7. Professor Robert L. Armstead, Code PHAR
Department of Physics
Monterey, California
8. Chairman, Physics Department, Code PHMW
Naval Postgraduate School
Monterey, California
9. Chairman, Electrical and Computer Engineering Department, Code ECPO
Naval Postgraduate School
Monterey, California
10. Engineering & Technology Curricular Office (Code 34)
Naval Postgraduate School
Monterey, California
11. CDR Roger McGinnis, USN
Naval Sea Systems Command
Washington D.C.

12. Dr. George Neil
TJNAF
Newport News, Virginia
13. Dr. Steve Benson
TJNAF/MS6A
Newport News, Virginia
14. Dr. Fred Dylla
TJNAF
Newport News, Virginia
15. Dr. Alan Todd
Advanced Energy System
Princeton, New Jersey
16. Dr. Dinh C. Nguyen
Los Alamos National Laboratory
Los Alamos, New Mexico
17. Professor Patrick G. O'Shea
Institute of Plasma Research and
Department of Electrical Engineering
Energy Research Facility, University of Maryland
18. Dr. Gil Graff
Office of Naval Research
Arlington, Virginia
19. Michael B. Deitchman
Office Naval Research
Arlington, Virginia
20. LT Vasileios Bouras H.N.
Athens, Greece